

# MTUQ: A framework for estimating moment tensors, point forces, and their uncertainties

J. Thurin<sup>1</sup>, R. Modrak<sup>2</sup>, C. Tape<sup>1</sup>, A. McPherson<sup>1</sup>, F. R. Rodriguez Cardozo<sup>3</sup>,  
J. Kintner<sup>2</sup>, L. Ding<sup>4,5</sup>, Q. Liu<sup>4</sup>, J. Braunmiller<sup>3</sup>

<sup>1</sup> *Geophysical Institute and Department of Geosciences, University of Alaska Fairbanks, Fairbanks, Alaska, 99775*,

<sup>2</sup> *Los Alamos National Laboratory,*

<sup>3</sup> *University of South Florida,*

<sup>4</sup> *University of Toronto,*

<sup>5</sup> *Geological Survey of Canada*

Received 1 October 2024

## SUMMARY

We introduce MTUQ, an open-source Python package for seismic source estimation and uncertainty quantification, emphasizing flexibility and operational scalability. MTUQ provides MPI-parallelized grid search and global optimization capabilities, compatibility with 1D and 3D Green's function database formats, customizable data processing, C-accelerated waveform and first-motion polarity misfit functions, and utilities for plotting seismic waveforms and visualizing misfit and likelihood surfaces. Applicability to a range of full- and constrained-moment tensor, point force, and centroid inversion problems is possible via a documented application programming interface (API), accompanied by example scripts and integration tests. We demonstrate the software using three different types of seismic events: 1) a 2009 intra-slab earthquake near Anchorage, Alaska; 2) an episode of the 2021 Barry Arm landslide in Alaska; and 3) the 2017 Democratic People's Republic of Korea (DPRK) underground nuclear test. With these events, we illustrate the well-known complementary character of body waves, surface waves, and

polarities for constraining source parameters. We also convey the distinct misfit patterns that arise from each individual data type, the importance of uncertainty quantification for detecting multi-modal or otherwise poorly constrained solutions, and the software's flexible, modular design.

**Key words:** Inverse theory – Earthquake source observations – Earthquake monitoring and test-ban treaty verification.

## 1 INTRODUCTION

Accurate estimation of seismic source parameters is important for understanding regional and global tectonic processes, assessing seismic hazards, and monitoring compliance with nuclear test-ban treaties. Two primary mathematical models used to represent seismic point sources are (1) the moment tensor, a second-order, symmetric tensor  $\mathbf{M} \in \mathbb{R}^{3 \times 3}$ , suitable for representing small- to moderate-sized seismic events (Aki & Richards, 2002); and (2) the point force  $\mathbf{f} \in \mathbb{R}^3$ , appropriate for mass movements such as landslides and volcanic eruptions (Kanamori & Given, 1982). Operationally, hundreds of inversions for such sources are carried out each day (e.g., Hayes et al. 2009; Herrmann et al. 2011; Ekström et al. 2012).

The moment tensor  $\mathbf{M}$  is defined as a symmetric second-order tensor that can be expressed as

$$\mathbf{M} = \mathbf{U}\Lambda\mathbf{U}^T, \quad (1)$$

where  $\mathbf{U}$  is the orthonormal matrix of eigenvectors ( $\mathbf{U}\mathbf{U}^T = \mathbf{I}$ ), which define the source orientation, and  $\Lambda$  is the diagonal matrix of eigenvalues ( $\lambda_1 \geq \lambda_2 \geq \lambda_3$ ), which describe the source type and magnitude. This provides a natural framework for source parameterization and visualization.

Accurate characterization of seismic sources remains challenging, despite the relatively low number of parameters required to define moment tensors or point forces. Low signal-to-noise ratios, inaccurate Earth models (e.g., Ford et al. 2009a; Duputel et al. 2014; Phạm & Tkalčić 2021; Hu et al. 2023), or tradeoffs between related source types (Ford et al., 2010) give rise to multi-modal or otherwise challenging misfit spaces. The misfit space for

small or sparsely observed events can exhibit multiple minima, causing conventional local-optimization methods to fail. Even for larger events recorded by many stations, the misfit surfaces over source type or orientation may exhibit complicated patterns that error bars, ellipses, or other simple methods fail to capture. Uncertainty analyses established by early studies provided a means to detect and quantify such misfit complexity (e.g., Riedesel & Jordan 1989; Valentine & Trampert 2012; Käufl et al. 2014; Stähler & Sigloch 2014). More recent geometric parameterizations (Tape & Tape, 2012, 2015, 2016) have made moment tensor uncertainty quantification easier, facilitating visualization of higher-dimensional spaces and reducing distortion in the projections.

We present MTUQ, a Python toolbox for seismic source estimation and uncertainty quantification that uses these new parameterizations to implement moment tensor and force parameter searches. MTUQ combines source parameter exploration with a flexible software design, in which users can adapt example scripts for common inversion tasks or implement fully customized workflows, drawing from an API that supports a variety of research avenues and operational applications.

MTUQ has been used in several studies (Thurin et al., 2022; Thurin & Tape, 2023; Delbridge et al., 2023; Kintner et al., 2023; Kumar et al., 2023), yet its design and capabilities have not yet been thoroughly discussed. Below, we first recall the formulation of source estimation as a function minimization problem, with optional “cut-and-paste” time shift corrections to account for Earth model errors (Zhu & Helmberger, 1996). We then describe MTUQ’s structure, features, and usage. Finally, we apply it to three test cases: (1) a moment tensor inversion for an intra-slab earthquake; (2) a point force inversion for an episode of the Barry Arm landslide in south-central Alaska; and (3) a moment tensor inversion for the 2017 Democratic People’s Republic of Korea nuclear test.

## 2 POINT SOURCE ESTIMATION

Point source estimation can be framed as a function minimization problem, in which we determine the seismic source  $\mathbf{s}$ —which is typically either a moment tensor  $\mathbf{M}$  or a force

$\mathbf{f}$ —that minimizes the misfit

$$\mathcal{C}(\mathbf{s}) = \sum_{r=1}^N \sum_{i=1}^3 \int_0^T [u_i(\mathbf{x}_r, t; \mathbf{s}) - u_i^{\text{obs}}(\mathbf{x}_r, t)]^2 dt, \quad (2)$$

between observed data  $u_i^{\text{obs}}(\mathbf{x}_r, t)$  and synthetic data  $u_i(\mathbf{x}_r, t; \mathbf{s})$ , with  $N$  denoting the number of stations,  $T$  the length of data window over time  $t$ , and  $u_i(\mathbf{x}_r, t)$  the  $i$ th component of the displacement at the  $r$ th station location  $\mathbf{x}_r$ . The misfit function here is written using the  $L_2$ -norm of the residuals, and other norms can alternatively be used.

The displacement response  $\mathbf{u}$  to a moment tensor  $\mathbf{M}$  or a point force  $\mathbf{f}$  at source location  $\mathbf{x}_s$  and origin time  $t_0$  is given by (Shearer, 2009)

$$u_i(\mathbf{x}, t; \mathbf{M}) = S(t) * \sum_{j=1}^3 \sum_{k=1}^3 M_{kj} \frac{\partial G_{ij}}{\partial (\mathbf{x}_s)_k}(\mathbf{x}, t, \mathbf{x}_s, t_0; \mathbf{V}), \quad (3)$$

or

$$u_i(\mathbf{x}, t; \mathbf{f}) = S(t) * \sum_{j=1}^3 f_j G_{ij}(\mathbf{x}, t, \mathbf{x}_s, t_0; \mathbf{V}), \quad (4)$$

respectively, where  $S(t)$  is the source-time function and  $G$  is the impulse response (i.e. Green's functions) of the Earth model  $\mathbf{V}$ .

In terms of Green's functions, the misfit function (Eq. 2) can be written concisely as

$$\mathcal{C}(\mathbf{s}) = \|\mathbf{u}^{\text{syn}} - \mathbf{u}^{\text{obs}}\|_2, \quad (5)$$

where  $\mathbf{u}^{\text{syn}}$  is obtained from the linear combination  $\mathcal{G}\mathbf{s}$ , and the temporal dependence and source time convolution having been made implicit. This concise formulation shows that the forward problem can be carried out using precomputed Green's function databases, as the synthetics become just a linear combination of Green's functions and source terms.

## 2.1 Uncertainty in the source characterization problem

Uncertainty in source estimation problems arises from data noise and model errors, while the source-receiver geometry influences the ability to resolve the source by affecting data coverage and sensitivity (e.g., azimuthal gap, stations aligned with the nodal plane of the source). While data noise is embedded in the observed data  $\mathbf{u}^{\text{obs}}$ , model error arises from limitations of  $\mathbf{V}$  which will not fully capture the Earth's physical properties, as well as

numerical errors in computing synthetics. In practice, Earth model limitations can be partly alleviated through the so-called “cut-and-paste” (CAP) method (e.g., Zhao & Helmberger 1994; Zhu & Helmberger 1996; Zhu & Ben-Zion 2013) at local and regional scales (typically within 0–20° distance). CAP works by partitioning waveforms into filtered and windowed body and surface wave phases and evaluating the misfit (5) between observations and time-shifted synthetics. Because at long periods, model error manifests primarily through phase misalignment, the CAP method can provide well-behaved long-period measurements and has become widely adopted in regional seismology. A common approach for determining the necessary time-shifts is to maximize the normalized cross-correlation coefficient:

$$\chi(t) = \frac{\int_{-\infty}^{\infty} u^{\text{obs}}(\tau)u(t+\tau)d\tau}{\left(\int_{-\infty}^{\infty}(u^{\text{obs}}(\tau))^2d\tau \int_{-\infty}^{\infty}(u(\tau))^2d\tau\right)^{1/2}}. \quad (6)$$

The maximum of  $\chi(t)$  usually occurs when the observed and synthetic waveforms are correctly aligned, but this may not be the case for nodal components or when cycle skipping occurs.

MTUQ allows users to evaluate the misfit function (5) either in its original form or using the cut-and-paste method, (i.e., with time-shifted synthetics based on 6). Because these misfit function evaluations are the most computationally expensive step in the whole parameter estimation problem, MTUQ provides highly-optimized misfit function implementations, as described in Section 3.

## 2.2 Parameter space exploration strategies

A simple but powerful way to estimate seismic point sources is to evaluate misfit at regular intervals over the source parameter space. Such searches may include source type, source orientation, magnitude, depth, centroid, and origin time parameters, resulting in grids of up to 10 dimensions. Evaluating the misfit function over the grid yields the minimum misfit solution along with the accompanying local and global structure of the misfit surface. In practice, we use the moment tensor parameterization proposed by Tape & Tape (2015) to construct grids that are either regularly spaced or randomly drawn from a uniform distri-

bution. Unlike the  $M_{ij}$  parameterization, Tape & Tape (2015)'s approach involves bounded ranges for source type and orientation, making it possible to avoid arbitrary lower and upper limits. (The source magnitude is still unbounded.) Evaluating the misfit function over individual grid points is an embarrassingly parallel problem, making it easy to implement on parallel systems, although limits posed by dimensionality make high-dimensional searches impractical.

For high-dimensional searches, we can turn to more efficient sampling strategies, which tend to prioritize low-misfit over high-misfit subsets of the parameter space. Among strategies that retain a grid structure, Xu et al. (2021) proposed a double-grid approach with coarse-to-fine grid search strategies. Another approach suggested by Lee et al. (2011) takes advantage of a coarse grid search and uses the best solution as the starting point for a Gauss-Newton iterative optimization method.

Another common strategy is to cast the moment tensor inversion problem in the Bayesian framework, using function-informed methods (e.g., Vackář et al. 2017; Pugh & White 2018; Pham & Tkalcic 2021; Hu et al. 2023) such as classical Markov chain Monte Carlo (MCMC) algorithms, or gradient-informed methods (Fichtner & Simute, 2018), such as Hamiltonian Monte Carlo (HMC). Given the challenges associated with convergence in Bayesian inversion, grid searches remain valuable as they provide a comprehensive benchmark for evaluating the accuracy and performance of these probabilistic approaches, particularly when exploring high-dimensional misfit surfaces. Grid searches are also the basis of formal uncertainty quantification which require a uniform sampling of the moment tensor space (Tape & Tape, 2016). As such, MTUQ's primary approach for source parameter estimation is based on exhaustive grid searches, offering a systematic and complete exploration of the parameter space.

Beyond grid searches, MTUQ's modular design accommodates advanced solvers as optional plugins. For example, the Covariance Matrix Adaptation Evolution Strategy (CMA-ES; Hansen & Ostermeier 2001; Hansen et al. 2015), a gradient-free global optimization method with self-tuning that has performed well in blind tests (Akimoto et al., 2010; Glas-

machers et al., 2010), has been successfully applied in prior source studies (Thurin et al., 2022; Thurin & Tape, 2023). It allows addressing higher-dimensional problems, such as joint inversion for source and centroid parameters or multiple sub-events characterization. MTUQ’s modular structure has also allowed us to pair it with a Hamiltonian Monte Carlo sampler (Ding et al., 2021) through SEISGen.

In this study, we expand on previous efforts (Thurin et al., 2022; Thurin & Tape, 2023) that applied new optimization methods to moment tensor inversion. Below, (Section 4.3) we present a combined workflow that uses CMA-ES, which we found to be especially promising, for initial source parameters estimation, followed by grid searches for quality control and uncertainty quantification.

### 3 SOFTWARE IMPLEMENTATION

MTUQ provides a flexible Python library for seismic source estimation and uncertainty quantification. Along with conventional  $l_1$  and  $l_2$  misfit evaluation, it implements the CAP algorithm of Zhu & Ben-Zion (2013) and its extensions (e.g., Silwal & Tape 2016; Alvizuri & Tape 2016; Alvizuri et al. 2018). Building on ObsPy and Instaseis data structures (Krischer et al., 2015; van Driel et al., 2015), MTUQ offers data misfit and data processing functions, local and remote Green’s function database clients, grid search and global optimization capabilities, and a range of visualization utilities. Customization is possible by either replacing default functions with user-defined ones or through a flexible frontend/backend architecture using object-oriented programming (e.g., subclassing).

MTUQ users define body-wave and surface-wave windows separately, allowing each set of windows to be weighted and normalized on its own. This approach prevents the inversion from being dominated by the large amplitudes of surface waves, while also allowing more control and flexibility on the misfit definition. Distinct preprocessing steps, such as bandpass filtering and time-shift corrections, can also be applied to each wave type. As shown by Zhu & Helmberger (1996), treating body and surface waves individually leverages their respective

sensitivities to different parts of the Earth’s structure and accounts for their strengths within differing frequency bands.

Waveform misfit functions are implemented with Cython acceleration (Behnel et al., 2011) and optional MPI parallelization, making them suitable for either consumer-grade or high-performance computing (HPC) systems and adaptable to both research and operational needs. MTUQ includes several implementations of misfit functions, ranging from readable, pure Python versions to optimized C/Python versions. The pure Python versions are useful for verifying the correctness of the more optimized ones. In addition to evaluating waveform misfit, MTUQ can use first-motion polarities comparing observed and predicted first motions to further constrain the source estimation. Misfit objects define various user-supplied options, such as the norm to use (L1, L2, or hybrid L1-L2), allowable time-shifts, and time-shift groupings (e.g., separating Rayleigh and Love waves by components). This flexible structure offers users fine-grained control over how different waveform types are treated in the inversion.

MTUQ supports the SAC data format (Goldstein et al., 2003) and makes extensive use of ObsPy data structures, with most operations on seismic traces handled by ObsPy *Stream()* and *Trace()* methods. In addition to providing seismic data, users can optionally provide a data weight file, which controls the relative contribution of individual stations and components to the overall data misfit. This weight file also allows for tuning body wave arrival times, static corrections (per-station correction to account for path effects larger than the allowable time-shift), and other windowing settings. Vertical and radial  $P$  waves, as well as vertical, radial, and transverse surface waves, can be adjusted independently. The effect of geometrical spreading can also be compensated via an amplitude scaling relationship based on distance (Zhu & Helmberger, 1996), which helps reduce the misfit contribution from amplitude decay that is otherwise unaccounted for. The weight files are designed with data sharing in mind, so that, when used with MTUQ library functions, data processing and misfit evaluation results can be reproduced.

Interfaces are provided for computing synthetics through elastic wave solvers and Green’s

function databases, including FK (Zhu & Rivera, 2002), AxiSEM (Nissen-Meyer et al., 2014), SPECFEM3D\_Cartesian (Komatitsch et al., 2004), SPECFEM3D\_GLOBE (Komatitsch & Tromp, 2002), and strain Green’s functions generated with SEISGen (Ding et al., 2021). If no local Green’s function databases are available, MTUQ can fetch Green’s tensors from the IRIS syngine web service (Krischer et al., 2017), which provides three-component AxiSEM-generated Green’s functions for periods as low as 2 seconds for various 1D Earth models.

Finally, utilities are provided for visualizing MTUQ grid search and global optimization results. Currently utilities are based on Matplotlib and optionally on Generic Mapping Tools (Wessel & Smith, 1991) and its Python interface PyGMT (Tian et al., 2024), with support for additional graphics backends possible through a frontend/backend architecture. Available functions include those for plotting misfit, likelihood, variance reduction, and tradeoffs (source-type vs. magnitude, source-type vs. depth) over point source parameters, as well as for visualizing how related station and trace attributes (such as misfit, time-shifts, normalized cross-correlation coefficient, and amplitude ratios) vary geographically. Using parameterizations from Tape & Tape (2012, 2015), we can plot marginal likelihood distributions over the moment tensor’s angular distance (Tape & Tape, 2016) and within the so-called  $v$ - $w$  space to quantify the probability that the true solution lies in the vicinity of the minimum misfit region.

The general MTUQ workflow is represented in Figure 1.

## 4 APPLICATIONS

We apply the MTUQ methods and software to three seismic events, highlighting some important practical issues. These examples include an intra-slab earthquake, a landslide, and the underground explosion resulting from the 2017 DPRK nuclear test. For the first event, we compare results obtained by searching over different combinations of source parameters and illustrate the main visualization capabilities. The second event demonstrates the code’s applicability to non-moment tensor cases, particularly in events involving mass movements.

Finally, the third example illustrates the flexible programmatic interface in a detailed comparison of source type derived from different seismic wave types and polarity data.

#### 4.1 Case 1 - 2009 intra-slab earthquake near Anchorage, Alaska

We begin with an event included in the MTUQ examples directory: a  $M_w$  4.6 intra-slab earthquake that occurred on April 7, 2009, north of Anchorage ( $61.45^\circ\text{N}$ ,  $149.74^\circ\text{W}$ ) at 20:12:55 UTC. This event was chosen for several reasons, including its magnitude (appropriate for a point source approximation), its data coverage, and because it was previously studied in Silwal & Tape (2016), which can serve as a baseline for comparison. Incidentally, this event also shares similarities in terms of location, orientation, and source type with the  $M_w$  7.1 earthquake that occurred on November 30, 2018 (West et al., 2019).

We perform three different inversions using a double-couple grid (DC), a deviatoric grid (DEV), and a full moment tensor grid (FULL), each including a magnitude search. The DC grid corresponds to the center point of the eigenvalue lune, the DEV grid covers the equator of the lune, and the FULL grid spans the entire lune (Figure 2c). This progression from DC to DEV to FULL grids reflects an increasing dimensionality of the source parameter space. The centroid depth is fixed at 33 km, based on the Alaska Earthquake Center catalog. We removed the instrument response and rotated the horizontal components to the radial and transverse directions for data processing. For this and all the following examples, we used ObsPy for data preprocessing and applied causal (one-pass) filters exclusively.

We use a 15 s window for  $P$  waves, bandpass filtered between [3, 16] s, and a 150 s window for surface waves, bandpass filtered between [16, 40] s. Both windows begin at the predicted (or manually picked) arrival time, determined using Taup-p (Crotwell et al., 1999) with a specified Earth model (in this case, ak135f Montagner & Kennett 1996). The allowable time shifts are  $\pm 2$  s for  $P$  waves and  $\pm 10$  s for surface waves, with Rayleigh and Love waves treated independently because they travel at different group velocities. We search for magnitude ranges from  $M_w$  4.4 to  $M_w$  4.7 over regular increments of  $M_w$  0.1.

In Figure 2, we show the waveform comparison figure headers output by MTUQ for the

three cases (DC, DEV, FULL). The headers list the best-fitting source and the inversion settings, including the solver and the Earth model. Because these settings are the same for all cases, differences between the best-fitting solution are related to the dimensionality of the source parameter space. We see that waveform misfit decreases with increasing grid dimensionality, as expected from the addition of free parameters. These results were obtained using the misfit function:

$$\mathcal{C}_w(\mathbf{M}) = \sum_{i=1}^n \left[ \mathbf{w}_{s,i} (\mathcal{G}_{s,i}\mathbf{M} - \mathbf{d}_{s,i}^{\text{obs}})^2 + \mathbf{w}_{p,i} (\mathcal{G}_{p,i}\mathbf{M} - \mathbf{d}_{p,i}^{\text{obs}})^2 \right], \quad (7)$$

where  $i = 1, \dots, n$  denotes the  $n$  source-receiver pairs,  $\mathcal{G}_{s,i}$  represents the  $i$ -th Green's function for the surface waves time-windows,  $\mathcal{G}_{p,i}$  represents the  $i$ -th Green's function for the  $P$ -wave time-windows, and  $\mathbf{M}$  is the moment tensor source term.  $\mathbf{d}_{s,i}^{\text{obs}}$  represents the  $i$ -th surface wave data and  $\mathbf{d}_{p,i}^{\text{obs}}$  is the  $i$ -th observed  $P$ -wave data. The terms  $\mathbf{w}_{s,i} \in \mathbb{R}^3$  and  $\mathbf{w}_{p,i} \in \mathbb{R}^2$  contain scalar weights applied to the residuals of the surface wave and  $P$ -wave windows, respectively.

Figure 3 illustrates the misfit-parameter tradeoffs as a function of double-couple orientation. For each pair of angles in a misfit map, we consider all possible third angle values and all possible magnitude values, and then we plot the lowest misfit associated with the best-fitting parameters. (Thus, the plots are not cross sections of the misfit function through parameter space.) The optimal solution (best orientation/angular triplet) is marked by a green circle across the three quadrants and corresponds to the value shown in the waveform plot figure header in Figure 2.

MTUQ also allows for the simultaneous inversion of both source parameters and location by expanding the grid dimension to include the source's coordinates in space. In this case, the full source-parameter grid will be evaluated for each source location (latitude, longitude, depth), enabling visualization of tradeoffs between source location and source parameters as shown in Figure 4 for depth. As searching for depth (or latitude and longitude) increases the dimensionality of the grid, it directly impacts the computational cost of the grid search method. In our experience, querying Green's functions is typically not the limiting factor

for grid search approaches, as the grid size is predefined and manageable. However, this can become a bottleneck for other optimization methods, such as CMA-ES or Hamiltonian Monte Carlo, where a larger number of sampled location points is often required. An example for conducting a centroid search is also bundled with the code but is not presented in this manuscript. For the sake of simplicity, we keep the catalog depth of 33 km for the subsequent results with this example event.

When moving to the full moment tensor grid, the source parameter space includes not only orientation parameters, but also source type parameters, which can be visualized using the eigenvalue lune (Tape & Tape, 2012). The misfit map over the eigenvalue lune contains insights about the tradeoffs between different source types, which can be useful for source discrimination (e.g., identifying explosions or collapses) or to assess the distance of an inversion outcome to the best double couple solution (Tape & Tape, 2019). Similar to the double-couple misfit maps, the lune misfit map is constructed by considering the best misfit value for each location on the lune, taking into account all possible orientations and magnitudes. The L2-norm based misfit map on the eigenvalue lune is displayed in Figure 5.

MTUQ also supports custom misfit functions  $\mathcal{C}(\mathbf{M})$ , such as joint waveform and first motion polarity misfit:

$$\mathcal{C}(\mathbf{M}) = \alpha \frac{\mathcal{C}_w(\mathbf{M})}{\|\mathbf{u}\|_2} + (1 - \alpha) \frac{\mathcal{C}_p(\mathbf{M})}{n_p}, \quad (8)$$

where  $\mathcal{C}_w(\mathbf{M})$  is the least-squares waveform misfit, normalized by the data norm  $\|\mathbf{u}\|_2$ ,  $\mathcal{C}_p(\mathbf{M})$  is the first-motion polarity misfit (expressed as the discrete number of mismatching polarities) over the number of observed first-motions  $n_p$ , and  $\alpha$  is a weighting factor that controls the relative contribution of waveform and polarity misfit terms, with  $\alpha = 1$  corresponding to purely normalized waveform misfit and  $\alpha = 0$  corresponding to purely polarity misfit. In Figure 6, we show the results for the DC, DEV, and FULL cases, with  $\alpha = 1$  and  $\alpha = 0.5$ . These results show the benefits of including first-motion polarities as an extra constraint in the inversion and highlight the advantages of customizable misfit functions. The results also differ from those obtained using the absolute misfit in Figure 2, as a consequence of modifying the misfit function, highlighting the importance of data normalization and weighting.

## 4.2 Case 2 - 2021 Barry Arm landslide

The following example involves a surface mass movement that occurred on the active Barry Arm landslide in south-central Alaska ( $61.24^{\circ}\text{N}$   $147.96^{\circ}\text{W}$ ) on August 9, 2021, at 07:45:50 UTC, featured as *Barry Arm 3* in Karasözen & West (2024). This event represents one of several detected movements at Barry Arm, highlighting the site's ongoing instability. The ability to determine force characteristics from seismic data is therefore a valuable tool for monitoring this and similar unstable slopes, particularly in remote locations where direct observations may be challenging. The point force approximation is generally favored over a moment tensor for representing a mass moving along an inclined surface. This model was introduced by Kanamori & Given (1982) to explain the surface wave radiation patterns recorded from the Mount St. Helens flank collapse (and subsequent explosion) during the 1980 volcanic eruption.

In this example, we consider data from 35 three-component broadband seismic stations, bandpass filtered between [16, 40] s, allowing a  $\pm 35$  s time-shift to account for imprecision in the onset time. The source depth is fixed at 0 km depth within the ak135f 1D Earth model (Montagner & Kennett, 1996). Due to the deficiency of short-period energy in the available data, the inversion was performed with surface waves only. Allowing a time-shift greater than a quarter of the dominant period of our waveforms can potentially introduce polarity-reversal biases (Braunmiller et al., 1994), which is present in the misfit map (Figure 7 b). We consider force amplitude in the range of  $10^{[9,12]}$  Newtons, with the exponent varying by 0.1 increments.

Figure 7a shows a subset of waveforms for the best-fitting point force, which points predominantly downward ( $\theta = 165^{\circ}$ ) with a bearing of  $\phi = 278^{\circ}$  (measured counter-clockwise from east). The downward direction might be explained by the steep slope of the Barry Arm landslide scarp. The best-fitting force is represented by a black diamond at the piercing point on the unit sphere. The associated misfit map is shown in Figure 7b. The ambiguity between upward and downward force arises from the polarity-reversal-bias, whereby a sign-flip of the force is accompanied by waveforms that are time-shifted by a quarter of a period. Reducing

the allowable time-shifts could help mitigate this effect, though it may come at the cost of flexibility in accommodating errors in the Earth model or onset timing, which can be challenging to evaluate in the case of a long duration, long-period signal.

### 4.3 Case 3 - 2017 DPRK nuclear test

On September 3, 2017 the Democratic People's Republic of Korea (DPRK) conducted an underground nuclear test at the Punggye-ri Nuclear Test Site. This test marked the largest ( $M_w$  5.24, Wang et al., 2018) in a series of six nuclear tests conducted over the previous years (Liu et al., 2018). A second, lower-magnitude event was detected 8.5 minutes after the main shock, likely due to a collapse at the test site (Alvizuri & Tape, 2018; Chiang et al., 2018), and background seismicity was observed in the weeks following the test (Tian et al., 2018).

The 2017 event has been extensively studied, as detailed in Table 2. Research efforts have focused on yield estimation (Lay, 2022; Stroujkova, 2018), event location (Myers et al., 2018; Pasmanos & Myers, 2018), and characterization of the source parameters and post-test collapse mechanism using advanced seismic analysis (Yao et al., 2018; Walter et al., 2018; Wang et al., 2018; Liu et al., 2018; Chiang et al., 2018; Alvezuri & Tape, 2018; Hong et al., 2019; Hu et al., 2023) and interferometric SAR imaging (Chi-Durán et al., 2021, 2024).

We revisit this event with a larger seismic dataset and a computationally-efficient workflow based on the CMA-ES algorithm in addition to the standard grid search method.

#### 4.3.1 *Data acquisition and processing*

The data used for this event include regional body waves, surface waves, polarities, and teleseismic polarities, which have all been included in previous studies, though not yet together (Table 2). While prior studies have used similar data types in various combinations, our workflow separates body- and surface-wave windows, weights each data type independently, and integrates polarities from both regional and teleseismic stations in a single inversion. By analyzing each data type separately, we investigate the source constraints each one provides and its respective contributions to the overall misfit surface.

For the body wave and surface wave analyses, we used waveforms from 31 regional stations within  $20^\circ$  of the epicenter ( $41.3^\circ$ ,  $129.078^\circ$ ) using only publicly available networks. The three-component regional data are bandpass filtered between 4–15 s for the body waves and 15–50 s for the surface waves. We used 25 s  $P$ -wave time windows, with the start times determined from the theoretical  $P$  waves arrival times using the  $TauP$  method (Crotwell et al., 1999) in the ak135f model (Montagner & Kennett, 1996). Surface wave time windows were set to 250 s with a start time controlled by a constant linear moveout of 3.8 km/s.

For the first-motion analysis, we added data from 153 teleseismic stations between  $20^\circ$  and  $100^\circ$ . We picked 10 first motions from the regional dataset and 46 polarities from the teleseismic dataset. All picked polarities were upward on the vertical raw (velocity) waveforms.

To efficiently generate synthetic waveforms, we worked with precomputed Green's functions simulated using the 1D model MDJ2 (Ford et al., 2009b), with a 1 s dominant period,  $20^\circ$  lateral extent, and 700 km depth extent. We used the spectral-element solver AxiSEM (Nissen-Meyer et al., 2007, 2014) for the Green's function simulations and Instaseis (van Driel et al., 2015) for subsequent synthetic seismogram generation.

To correct phase misalignment biases (i.e., cycle skipping), we employed a two-step process. First, we performed a preliminary inversion that allowed for large time-shifts across all stations to identify systematic delays. Time-shift corrections were then derived by ensuring geographic consistency in the distribution of time-shifts and by visually inspecting waveform fits for evidence of phase misalignment. This step confirmed that eastward oceanic paths toward Japan required up to 30 s of static corrections (Alvizuri & Tape, 2018), while the continental paths—including to station MDJ—did not require any static correction. The custom static corrections were applied to selected stations to limit allowable time-shifts during the final inversion to  $\pm 2$  s for  $P$ -waves and  $\pm 10$  s for surface waves. The combination of static corrections and shorter allowable time shifts reduces computational cost and reduces the emergence of local minima having a source mechanism flipped in sign from the true solution.

### 4.3.2 Method

We use CMA-ES, which was previously used to invert multiple sub-sources of the 2022 Hunga Tonga-Hunga Ha'apai volcanic eruption (Thurin et al., 2022; Thurin & Tape, 2023). Here, we present a simpler analysis using only a single source, which demonstrates how initial CMA-ES model space exploration can be used with subsequent grid searches as part of an efficient combined workflow.

In practice, we find that it cost-effective to explore a large range of depths and magnitudes using CMA-ES, from which a smaller range can be selected for subsequent grid searches. In addition to being computationally efficient, CMA-ES is well-suited for problems where model parameters (e.g., magnitude, source type, source orientation, and location) have different scales or units. Unlike grid search methods, it operates over continuous parameter spaces rather than a predefined discrete set.

Our CMA-ES implementation follows Hansen (2016), with the addition of boundary-handling constraint methods from Biedrzycki (2020). Specifically, we implement a periodic boundary for the strike angle and point force bearing (which varies from  $0^\circ$  to  $360^\circ$  and can wrap around these limits) and a randomized redraw for other out-of-bound samples. A short review of the CMA-ES algorithm can be found in Appendix A of Thurin & Tape (2023). We use a population of 64 samples in each CMA-ES iteration, and run the algorithm for 180 iterations (fixed), for a total of 11,520 function evaluations. We then conduct a fine-scale grid search, which included a total of  $5.977 \times 10^7$  grid points, using the magnitude estimate from the CMA-ES inversion. We fix the source centroid at  $41.30^\circ\text{N}$ ,  $129.08^\circ\text{E}$ , and 1 km depth.

### 4.3.3 Results for a moment tensor

The misfit map obtained from 180 iterations of CMA-ES is displayed in Figure 8, which reveals how CMA-ES focuses preferentially on regions with low misfit. Once CMA-ES identifies a descent direction, most subsequent samples are clustered in the upper portion of the eigenvalue lune, consistent with an isotropic (explosive) source.

The source that minimizes the misfit for our combined dataset is an explosion-like moment tensor, with  $M_w$  5.44, determined by optimizing over a continuous magnitude range of  $M_w$  [5.1–5.9]. This result then informs the subsequent grid search, narrowing the magnitude range to  $M_w$  [5.42, 5.44, 5.46]. This focused approach prevents searching over an unnecessary large parameter space. In this way, the CMA-ES results serve as a prior constraint for the grid search. We perform the two-part inversions (CAM-ES and grid-search) using regional body waves (BW), regional surface waves (SW), regional first-motion polarities (RP), and teleseismic first-motion polarities (TP) with equal weights ( $w = 0.25$ ) to ensure a balanced contribution to the normalized joint misfit.

Figure 9 shows the best-fitting moment tensor and a selection of waveform fits from the fine grid search. Since each misfit is evaluated independently, MTUQ allows us to combine them in a post-processing stage, enabling the computation of misfit maps for multiple scenarios once the grid search is complete, as shown in Figure 10. From left to right, the figure shows the normalized misfit for [BW] alone, [SW] alone, the combination of [BW, SW], [BW, SW, RP], and finally, the combination of [BW, SW, RP, TP]. Underneath each misfit map, we plotted the confidence curve (Tape & Tape, 2016) for a fixed magnitude (from the optimal value of  $M_w$  5.44) and a uniform random grid. Specifically, the probability density function is expressed as:

$$p(\mathbf{M}) = \frac{s(\mathbf{M})}{\int_{\mathcal{M}} s(\mathbf{M}) d\mathbf{M}}, \quad \text{where} \quad s(\mathbf{M}) = \exp\left(-\frac{\mathcal{C}(\mathbf{M})}{2\sigma^2}\right), \quad (9)$$

where  $\mathbf{M}_0$  is the best-fitting moment tensor, and  $\mathcal{M}$  represents the sample space.

The parameter  $\sigma$  represents the estimated standard deviation of the data errors, which is estimated differently for waveform and polarity data. For waveform misfits, it is determined by evaluating the standard deviation of the residual of the best fitting solution. For polarity data,  $\sigma$  is estimated via a Beta-binomial update that incorporates the frequency of observed polarity mismatches. We begin with an uninformative  $Beta(1, 1)$  prior on the mismatch probability, which is then updated to a posterior distribution based on the number of observed mismatches. This procedure regularizes the estimate of  $\sigma$  by incorporating prior uncertainty

and thereby prevents  $\sigma$  from collapsing to zero. When combining misfits from different data groups, we normalize each misfit by dividing it by the norm of its corresponding observed data vector, then take the arithmetic mean of these normalized misfits. The total variance is obtained by summing the individual variances, each scaled by its corresponding data norm.

As we add data constraints, the area of low misfit reduces, thereby lowering the uncertainty of the results (Figure 10). This impacts the shape of the confidence curves, which evolve toward a  $\Gamma$ -like shape having a larger area under the curve and, hence, a larger confidence parameter  $P_{AV}$ . Although polarities alone may not be sufficient to determine a unique best-fitting solution, they significantly contribute when combined with waveform data (Ford et al., 2012; Chiang et al., 2014; Alvizuri et al., 2018; Chi-Durán et al., 2021, 2024). Moreover, including both regional and teleseismic polarities appears beneficial, as the rightmost misfit map (Figure 10) has the narrowest and tightest low misfit region of all maps (even though the confidence parameter only increases marginally when including teleseismic polarities). The complete set of figures for the 5 inversions can be found in supplementary figures S14 to S25.

It is helpful to visualize variations in station attributes on a map, illustrating how azimuths, distance, or site effects might affect the inversion outcome. The time-shift maps in Figure 11 highlight the need for time-shift corrections, as all the paths crossing the Sea of Japan require up to  $-30$  seconds time-shifts in the MDJ2 model, which is consistent with observations in Dreger et al. (2021). Notably, Rayleigh wave time-shifts demonstrate strong azimuthal coherence across the Sea of Japan, whereas Love wave time-shifts show more variability. This variation in Love wave time-shifts might be attributed to the generally lower signal-to-noise ratio in the horizontal components of the waveforms or to the shallower crustal sensitivity of Love waves.

#### *4.3.4 Results for a point force*

The previous results demonstrate that an all-positive-eigenvalue moment tensor can fit the considered seismic datasets. Motivated by the ambiguity between shallow explosive-like mo-

ment tensors and a vertical downward force applied to the Earth's surface in volcanic explosions (Kanamori & Given, 1982), we perform a point force inversion of the DPRK nuclear test. Using the same datasets as in Section 4.3.3, we perform a grid search over all force orientations, with a force amplitude in the range of  $10^{[10,14]}$  Newtons, with the exponent varying by 0.1 increments, and again at a fixed depth of 1 km and assuming the MDJ2 1D Earth model. Since the point force grid is much smaller than the full moment tensor grid, using CMA-ES here is less advantageous, and we can directly search with a fine amplitude increment instead.

The waveform fits obtained from the joint inversion of [BW, SW, RP, TP] and associated misfit maps are shown in the supplementary material figures S29 and S30. The source that best fits the dataset is a downward force, with waveform fits that are qualitatively comparable to the moment tensor solution (albeit a higher absolute waveform misfit).

This result suggests that these two models—moment tensor and point force—can both explain the seismic recordings from anthropogenic explosions and from volcanic explosions, as documented by Thurin & Tape (2023) for the Hunga Tonga-Hunga Ha'apai volcanic eruption. The canonical models (moment tensor, force) in their respective fields contribute to this ambiguity. The main feature that distinguishes these two models are the near-field, high-frequency waveforms, and the Love wave radiation patterns: two-lobed for a point force (Kanamori et al., 1984) and four-lobed for a moment tensor. In practice, resolving this ambiguity is challenging due to limited data availability and to the weak amplitudes typically associated with shallow explosive sources. Note that the two conceptual models have been combined into a compound source model in Hu et al. (2024), where a vertical force and an isotropic moment tensor source are shown to explain the main seismic source of the 2022 Hunga Tonga volcanic sequence, highlighting the interest in discriminating source models in complex geophysical settings.

## 5 DISCUSSION

We presented three distinct applications: an earthquake, a landslide event, and an underground nuclear explosion. The first two cases draw directly from the examples packaged with the software itself, while the third case illustrates a more involved workflow, combining multiple software elements in a new way to understand the contributions from different data types to overall seismic source constraints.

Layered (1D) models often produce satisfactory results within the context of the cut-and-paste method (particularly if using long-period data), but their limitations become evident when large time-shifts are required to align observed and synthetic waveforms at specific stations or azimuthal ranges, as seen for stations across the Sea of Japan in the DPRK test (Figure 11). These large time-shifts highlight the inadequacy of using a single 1D models in capturing all path-dependent effects. Although manual adjustments can mitigate these issues, they underscore the need for more sophisticated modeling approaches. MTUQ is compatible with 3D Green's function databases derived from numerical solvers such as SPECFEM3D (or SEISGen for Strain Green's functions), offering a pathway to improve forward modeling accuracy in regions with complex structures, where the importance of accounting for 3D effects has been well-demonstrated (Ramos-Martínez & McMechan, 2001; Liu et al., 2004; Covellone & Savage, 2012; Hejrani et al., 2017; Takemura et al., 2020; Sawade et al., 2022)

Previous studies and ongoing efforts have integrated 3D Green's functions with MTUQ using its existing interfaces, both for source-side moment tensor inversions (Rodriguez Cardozo et al., 2022; McPherson et al., 2023) and for receiver-side moment tensor inversions (Ding et al., 2021), which requires saving the time-dependent volumetric wavefield within a target source region. These studies have leveraged 3D Green's functions to validate expected improvements, including better waveform fits, reduced time-shifts, and moment tensor solutions that align more closely with double-couple mechanisms for tectonic earthquakes.

However, one challenge with many existing 3D Earth models is that they rely predominantly on long-period seismic data, and higher-resolution models need to be developed

to improve waveform fitting in the 15–40 s period range relevant for most regional moment tensor applications. Another challenge is the relatively limited understanding of how uncertainties in 3D Earth models propagate into moment tensor solutions. While model uncertainties have been studied in 1D contexts (Yagi & Fukahata, 2011; Duputel et al., 2014; Pham & Tkalcic, 2021), their treatment in 3D inversion frameworks is under active study (Pham et al., 2024). Future work in this area is critical to ensure that the improved accuracy provided by 3D models is accompanied by robust uncertainty quantification. A secondary advantage of incorporating 3D Earth models is the potential to reduce tradeoffs between the centroid and time-shifts. Working directly with 3D models should improve joint inversions of centroid and source mechanism parameters (Takemura et al., 2020; Ding et al., 2021).

Another key aspect of MTUQ is its compatibility with multiple inversion strategies, allowing users to go beyond exhaustive grid searches for parameter estimation. While grid searches provide a complete exploration of the parameter space, they become computationally expensive as the dimensionality of the problem increases. For example, performing a joint inversion of source parameters and centroid locations dramatically expands the search space. Alternative optimization strategies like the CMA-ES or HMC offer significant computational advantages: CMA-ES can be used as an efficient alternative to grid search when parallel computational resources are not available. These methods, already integrated into MTUQ via compatible plug-ins, are well-suited for exploring misfit spaces with a few dozen of parameters. Pairing these global optimization approaches with refined grid searches, as illustrated in Case 3 (Section sec:case3), enables users to focus computational efforts on the most promising regions of the parameter space. These efficient techniques provide opportunities to explore novel applications, such as multi-event inversions or real-time monitoring.

Another promising avenue for future development lies in expanding MTUQ’s capabilities to handle compound sources (combinations of moment tensor and single force). This extension would potentially allow the framework to discriminate “exotic” events types—such as shallow volcanic explosions, landslides, or exotic anthropogenic sources—from regular earthquakes. Such a compound source model has been used to invert a potential model for the

2022 eruption of the Hunga Tonga volcano (Hu et al., 2024) and would enhance MTUQ's ability to deal with data from complex geophysical processes. These developments are important for improving source discrimination in challenging scenarios where mixed source mechanisms contribute to the observed seismicity, such as volcanic eruptions with mass movements or shallow explosions producing secondary collapses.

## 6 CONCLUSION

We have reviewed the design and capabilities of MTUQ, an open-source software package for seismic source estimation and uncertainty quantification. Through three test cases, we illustrated how the code can be applied to moment tensor and point source estimation problems. Other recent efforts have illustrated additional capabilities and use cases, such as for earthquake seismology (Mahanta et al., 2024), planetary seismology (Maguire et al., 2023), and volcano seismology (Thurin et al., 2022; Thurin & Tape, 2023; Kintner et al., 2022).

We aim to continue adding features, such as better ways of accounting for data and model covariance, support for compound sources (combinations of force and moment tensors), and the ability to model multiple moment tensors from different locations with slight time shifts to capture multi-event or subevent scenarios. We also hope to continue offering virtual and hybrid workshops to attract and sustain MTUQ users. Previous efforts include the 2022 MTUQ virtual workshop and the tutorials at the 2024 SCOPED workshop (Denolle et al., 2025).

In summary, MTUQ provides a flexible source inversion toolbox aimed at both research and operational applications. For reference, the datasets and scripts used for Cases 1 and 2 above are bundled directly with the package.

## DATA AVAILABILITY

- Scripts for reproducing the grid-search results and figures from Cases 1 to 3, along with the best-fitting moment tensor parameters, weight files, first-motion polarity picks, and data

for Case 3, are available in the Zenodo collection at (<https://doi.org/10.5281/zenodo.13868450>).

- The github organization MTUqorg at <https://github.com/mtuqorg> contains the moment tensor code, MTUQ, including bundled data for Case 1 (Silwal & Tape, 2016) and Case 2 (Karasözen & West, 2024).

MTUQorg contains other modules for MTUQ, including SeisHMC and SEISGen, for performing receiver-side source estimation using 3D Strain Green’s functions (Ding et al., 2021). The module `mtuq_cmaes` features the CMAES approach for sampling model parameter space (Section 4.3.2).

The package Pysep was used for fetching observed waveforms and for preprocessing; it is available at <https://github.com/adjtomo/pysep>.

- Seismic waveform data used in this study are from the AK, AT, AV, G, IC, II, IU, JP, KG, KS, TW, and YV networks (<https://www.fdsn.org/networks>, last accessed August 2023), and they were accessed via the EarthScope Data Management Center.
- For the DPRK inversion (Section 4.3.3), we did not use the DB network stations featured in Wang et al. (2018), because we were unable to obtain the correct metadata needed to remove the instrument response.

## ACKNOWLEDGMENTS

We thank Editor Andrew Valentine and the reviewers—Arthur Rodgers and an anonymous reviewer—for their helpful comments, feedback, and suggestions. We thank the University of Alaska Fairbanks (UAF) Research Computing Systems for an allocation on the “chinook” high-performance computing cluster. This project was supported by Air Force Research Laboratory contract HQ0034-20-F-0284 and the TREMOR project by contract FA9453-24-9-0001, with management support from the UAF Geophysical Detection of Nuclear Proliferation (GDNP) University Affiliated Research Center (UARC). MTUQ is featured in the SCOPED project, which is supported by NSF Award OAC 2104052. We thank Ezgi Karasözen and Michael West for recommending the Barry Arm landslide event in Section 4.2

and for curating the dataset. We thank Tom VanDeMark, Aileen Fisher, Robert Walker, and Mike Cleveland for useful discussions that helped improve the usability of the package.

## References

- Aki, K. & Richards, P. G., 2002. *Quantitative Seismology*, University Science Books, San Francisco, Calif., USA, 2nd edition., 2009 corrected printing.
- Akimoto, Y., Nagata, Y., Ono, I., & Kobayashi, S., 2010. Bidirectional Relation between CMA Evolution Strategies and Natural Evolution Strategies, in *Parallel Problem Solving from Nature, PPSN XI*, pp. 154–163, Springer Berlin Heidelberg.
- Alvizuri, C. & Tape, C., 2016. Full moment tensors for small events ( $M_w < 3$ ) at Uturuncu volcano, Bolivia, *Geophys. J. Int.*, **206**, 1761–1783, doi: 10.1093/gji/ggw247.
- Alvizuri, C. & Tape, C., 2018. Full moment tensor analysis of nuclear explosions in North Korea, *Seismol. Res. Lett.*, **89**(6), 2139–2151, doi: 10.1785/0220180158.
- Alvizuri, C., Silwal, V., Krischer, L., & Tape, C., 2018. Estimation of full moment tensors, including uncertainties, for nuclear explosions, volcanic events, and earthquakes, *J. Geophys. Res. Solid Earth*, **123**, 5099–5119, doi: 10.1029/2017JB015325.
- Behnel, S., Bradshaw, R., Citro, C., Dalcin, L., Seljebotn, D. S., & Smith, K., 2011. Cython: The best of both worlds, *Computing in Science & Engineering*, **13**(2), 31–39.
- Biedrzycki, R., 2020. Handling bound constraints in CMA-ES: An experimental study, *Swarm and Evolutionary Computation*, **52**, 100627, doi: <https://doi.org/10.1016/j.swevo.2019.100627>.
- Braunmiller, J., Dahm, T., & Bonjer, K.-P., 1994. Source mechanism of the 1992 Roermond earthquake from surface-wave inversion of regional data, *Geophys. J. Int.*, **116**(3), 663–672, doi: 10.1111/j.1365-246X.1994.tb03288.x.
- Chi-Durán, R., Dreger, D. S., Rodgers, A. J., & Nayak, A., 2021. Joint regional waveform, first-motion polarity, and surface displacement moment tensor inversion of the 3 September 2017 North Korean nuclear test, *The Seismic Record*, **1**(2), 107–116, doi: 10.1785/0320210022.

- Chi-Durán, R., Dreger, D. S., & Rodgers, A. J., 2024. Joint inversion of regional waveform, first-motion polarity, and synthetic aperture radar surface displacement for the fourth and sixth North Korean declared nuclear explosions, *Bull. Seismol. Soc. Am.*, **114**, 2409–2423, doi: 10.1785/0120230237.
- Chiang, A., Dreger, D. S., Ford, S. R., & Walter, W. R., 2014. Source characterization of underground explosions from combined regional moment tensor and first-motion analysis, *Bull. Seismol. Soc. Am.*, **104**(4), 1587–1600, doi: 10.1785/0120130228.
- Chiang, A., Ichinose, G. A., Dreger, D. S., Ford, S. R., Matzel, E. M., Myers, S. C., & Walter, W. R., 2018. Moment tensor source-type analysis for the Democratic People's Republic of Korea-declared nuclear explosions (2006–2017) and 3 September 2017 collapse event, *Seismol. Res. Lett.*, **89**(6), 2152–2165, doi: 10.1785/0220180130.
- Covellone, B. M. & Savage, B., 2012. A quantitative comparison between 1D and 3D source inversion methodologies: Application to the Middle East, *Bull. Seismol. Soc. Am.*, **102**(5), 2189–2199, doi: 10.1785/0120110278.
- Crotwell, H. P., Owens, T. J., & Ritsema, J., 1999. The TauP Toolkit: flexible seismic travel-time and ray-path utilities, *Seismol. Res. Lett.*, **70**(2), 154–160.
- Delbridge, B. G., Carmichael, J. D., Phillips, W. S., Cleveland, K. M., Begnaud, M. L., & Gammans, C., 2023. Source characterization of the declared North Korean nuclear tests from regional distance coda wave spectral ratios, *J. Geophys. Res. Solid Earth*, **128**, 1–32, doi: 10.1029/2022JB024728.
- Denolle, M., Tape, C., Bozdağ, E., Wang, Y., Waldhauser, F., Gabriel, A.-A., Braumiller, J., Chow, B., Ding, L., Feng, K.-F., Ghosh, A., Groebner, N., Gupta, A., Krauss, Z., McPherson, A. M., Nagaso, M., Niu, Z., Ni, Y., Örsvuran, R., Pavlis, G., Rodriguez-Cardozo, F., Sawi, T., Schliwa, N., Schneller, D., Shi, Q., Thurin, J., Wang, C., Wang, K., Wing Ching Wong, J., Wolf, S., & Yuan, C., 2025. Training the next generation of seismologists: Delivering research-grade software education for Cloud and HPC computing through diverse training modalities, *Seismol. Res. Lett.* (preprint; in review), doi: 10.48550/arXiv.2409.19147.

- Ding, L., Liu, T., Wang, K., He, B., Yang, G., Lei, T., Tape, C., Thurin, J., Grasselli, G., & Liu, Q., 2021. Simultaneous inversion and uncertainty analysis of moment tensor and source location based on 3D strain Green's function database computed by spectral-element methods: with applications to the 2019 Ridgecrest sequence, Abstract S51B-06 presented at 2021 Fall Meeting, AGU, 13-17 Dec.
- Dreger, D. S., Gritto, R., & Nelson, O., 2021. Path Calibration of the Democratic People's Republic of Korea 3 September 2017 Nuclear Test, *Seismol. Res. Lett.*, **92**(6), 3375–3385, doi: 10.1785/0220210105.
- Duane, S., Kennedy, A., Pendleton, B. J., & Roweth, D., 1987. Hybrid Monte Carlo, *Physics Letters B*, **195**(2), 216–222, doi: [https://doi.org/10.1016/0370-2693\(87\)91197-X](https://doi.org/10.1016/0370-2693(87)91197-X).
- Duputel, Z., Agram, P. S., Simons, M., Minson, S. E., & Beck, J. L., 2014. Accounting for prediction uncertainty when inferring subsurface fault slip, *Geophysical Journal International*, **197**(1), 464–482, doi: 10.1093/gji/ggt517.
- Ekström, G., Nettles, M., & Dziewoński, A. M., 2012. The global GCMT project 2004–2010: Centroid-moment tensors for 13,017 earthquakes, *Phys. Earth Planet. Inter.*, **200-201**, 1–9, doi: 10.1016/j.pepi.2012.04.002.
- Fichtner, A. & Simute, S., 2018. Hamiltonian Monte Carlo inversion of seismic sources in complex media, *J. Geophys. Res. Solid Earth*, **123**, 2984–2999, doi: 10.1002/2017JB015249.
- Ford, S. R., Dreger, D. S., & Walter, W. R., 2009a. Identifying isotropic events using a regional moment tensor inversion, *J. Geophys. Res.*, **114**, doi: 10.1029/2008JB005743.
- Ford, S. R., Dreger, D. S., & Walter, W. R., 2009b. Source analysis of the Memorial Day explosion, Kimchaek, North Korea, *Geophys. Res. Lett.*, **36**(21), doi: 10.1029/2009GL040003.
- Ford, S. R., Dreger, D. S., & Walter, W. R., 2010. Network sensitivity solutions for regional moment-tensor inversions, *Bull. Seismol. Soc. Am.*, **100**(5A), 1962–1970, doi: 10.1785/0120090140.
- Ford, S. R., Walter, W. R., & Dreger, D. S., 2012. Event discrimination using regional moment tensors with teleseismic-*P* constraints, *Bull. Seismol. Soc. Am.*, **102**(2), 867–

872, doi: 10.1785/0120110227.

Glasmachers, T., Schaul, T., Yi, S., Wierstra, D., & Schmidhuber, J., 2010. Exponential natural evolution strategies, in *Proceedings of the 12th Annual Conference on Genetic and Evolutionary Computation*, GECCO '10, p. 393–400, Association for Computing Machinery, doi: 10.1145/1830483.1830557.

Goldstein, P., Dodge, D., Firpo, M., & Minner, L., 2003. SAC2000: Signal processing and analysis tools for seismologists and engineers, in *International Handbook of Earthquake and Engineering Seismology*, vol. 81B of **International Geophysics Series**, pp. 1613–1614, eds Lee, W. H. K., Kanamori, H., Jennings, P. C., & Kisslinger, C., Academic Press.

Hansen, N., 2016. The CMA evolution strategy: A tutorial, <https://doi.org/10.48550/arXiv.1604.00772>.

Hansen, N. & Ostermeier, A., 2001. Completely Derandomized Self-Adaptation in Evolution Strategies, *Evolutionary Computation*, **9**(2), 159–195, doi: 10.1162/106365601750190398.

Hansen, N., Arnold, D. V., & Auger, A., 2015. Evolution strategies, in *Springer Handbook of Computational Intelligence*, eds Kacprzyk, J. & Pedrycz, W., Berlin, doi: 10.1007/978-3-662-43505-2\_44.

Hayes, G., Rivera, L., & Kanamori, H., 2009. Source inversion of the W-phase: real-time implementation and extension to low magnitudes, *Seismol. Res. Lett.*, **80**(5), 817–822, doi: 10.1785/gssrl.80.5.817.

Hejrani, B., Tkalcic, H., & Fichtner, A., 2017. Centroid moment tensor catalogue using a 3-D continental scale Earth model: Application to earthquakes in Papua New Guinea and the Solomon Islands, *J. Geophys. Res. Solid Earth*, **122**(7), 5517–5543, doi: <https://doi.org/10.1002/2017JB014230>.

Herrmann, R. B., Benz, H., & Ammon, C. J., 2011. Monitoring the earthquake source process in North America, *Bull. Seismol. Soc. Am.*, **101**(6), 2609–2625, doi: 10.1785/0120110095.

Hong, T.-K., Lee, J., Park, S., Yoon, H. H., Kim, W., & Shin, J. S., 2019. Seismic detection

- of strong ground motions by MW 5.6 North Korean nuclear explosion, *Scientific Reports*, **9**(1), 5124, doi: <https://doi.org/10.1038/s41598-019-41627-x>.
- Hu, J., Pham, T.-S., & Tkalčić, H., 2023. Seismic moment tensor inversion with theory errors from 2-D Earth structure: implications for the 2009–2017 DPRK nuclear blasts, *Geophys. J. Int.*, **235**, 2035–2054, doi: [10.1093/gji/ggad348](https://doi.org/10.1093/gji/ggad348).
- Hu, J., Phạm, T.-S., & Tkalčić, H., 2024. A composite seismic source model for the first major event during the 2022 Hunga (Tonga) volcanic eruption, *Geophys. Res. Lett.*, **51**, 1–11, doi: [10.1029/2024GL109442](https://doi.org/10.1029/2024GL109442).
- Kanamori, H. & Given, J. W., 1982. Analysis of long-period seismic waves excited by the May 18, 1980, eruption of Mount St. Helens – A terrestrial monopole?, *J. Geophys. Res.*, **87**(B7), 5422–5432.
- Kanamori, H., Given, J. W., & Lay, T., 1984. Analysis of seismic body waves excited by the Mount St. Helens eruption of May 18, 1980, *J. Geophys. Res.*, **89**(B3), 1856–186.
- Karasözen, E. & West, M. E., 2024. Toward the Rapid Seismic Assessment of Landslides in Coastal Alaska, *The Seismic Record*, **4**(1), 43–51, doi: [10.1785/0320230044](https://doi.org/10.1785/0320230044).
- Käufel, P., Valentine, A. P., O'Toole, T. B., & Trampert, J., 2014. A framework for fast probabilistic centroid-moment-tensor determination—inverson of regional static displacement measurements, *Geophys. J. Int.*, **196**, 1676–1693, doi: [10.1093/gji/ggt473](https://doi.org/10.1093/gji/ggt473).
- Kintner, J. A., Yeck, W. L., Earle, P. S., Prejean, S., & Pesicek, J., 2022. High-precision characterization of seismicity from the 2022 Hunga Tonga-Hunga Ha'apai volcanic eruption, *Seismol. Res. Lett.*, **94**, 589–602, doi: [10.1785/0220220250](https://doi.org/10.1785/0220220250).
- Kintner, J. A., Cleveland, K. M., Pippin, J. A., Modrak, R. T., & Delbridge, B., 2023. Time-varying moment-tensor analysis with application to buried chemical explosions, *Seismol. Res. Lett.*, **95**, 352–366, doi: [10.1785/0220230139](https://doi.org/10.1785/0220230139).
- Komatitsch, D. & Tromp, J., 2002. Spectral-element simulations of global seismic wave propagation—II. Three-dimensional models, oceans, rotation and self-gravitation, *Geophys. J. Int.*, **150**, 308–318.
- Komatitsch, D., Liu, Q., Tromp, J., Süss, P., Stidham, C., & Shaw, J. H., 2004. Simulations

- of ground motion in the Los Angeles basin based upon the spectral-element method, *Bull. Seismol. Soc. Am.*, **94**(1), 187–206, doi: 10.1785/0120030077.
- Krischer, L., Mengies, T., Barsch, R., Beyreuther, M., Lecocq, T., Caudron, C., & Wassermann, J., 2015. ObsPy: a bridge for seismology into the scientific Python ecosystem, *Computational Science & Discovery*, **8**(1), 1–17, doi: 10.1088/1749-4699/8/1/014003.
- Krischer, L., Hutko, A. R., van Driel, M., Stähler, S., Bahavar, M., Trabant, C., & Nissen-Meyer, T., 2017. On-demand custom broadband synthetic seismograms, *Seismol. Res. Lett.*, **88**(4), 1127–1140, doi: 10.1785/0220160210.
- Kumar, P., Silwal, V., Mahanta, R., Maurya, V. K., Kamal, Sharma, M. L., & Ammani, A., 2023. Near real-time detection and moment tensor inversion of the 11 May 2022, Dharchula earthquake, *GeoHazards*, **4**, 515–525, doi: 10.3390/geohazards4040029.
- Lay, T., 2022. Direct Estimation of Explosion Pn Green's Functions Applied to Teleseismic P-wave Intercorrelations for North Korean Nuclear Tests, *The Seismic Record*, **2**(1), 11–19, doi: 10.1785/0320210045.
- Lee, E.-J., Chen, P., Jordan, T. H., & Wang, L., 2011. Rapid full-wave centroid moment tensor (CMT) inversion in a three-dimensional earth structure model for earthquakes in Southern California, *Geophys. J. Int.*, **186**(1), 311–330, doi: 10.1111/j.1365-246X.2011.05031.x.
- Liu, J., Li, L., Zahradník, J., Sokos, E., & Plicka, V., 2018. Generalized source model of the North Korea tests 2009–2017, *Seismol. Res. Lett.*, **89**(6), 2166–2173, doi: 10.1785/0220180106.
- Liu, Q., Polet, J., Komatitsch, D., & Tromp, J., 2004. Spectral-element moment tensor inversions for earthquakes in southern California, *Bull. Seismol. Soc. Am.*, **94**(5), 1748–1761, doi: 10.1785/012004038.
- Maguire, R., Lekić, V., Kim, D., Schmerr, N., Li, J., Beghein, C., Huang, Q., Irving, J. C. E., Karakostas, F., Lognonné, P., Stähler, S. C., & Banerdt, W. B., 2023. Focal mechanism determination of event S1222a and implications for tectonics near the dichotomy boundary in southern Elysium Planitia, Mars, *J. Geophys. Res. Solid Earth*, **128**, 1–13,

doi: 10.1029/2023JE007793.

- Mahanta, R., Silwal, V., & Sharma, M. L., 2024. Body waves– and surface waves–derived moment tensor catalog for Garhwal-Kumaon Himalayas, in *Recent Developments in Earthquake Seismology*, pp. 47–63, eds Singh, R., Kanhaiya, S., & Maurya, S. P., Springer, Cham, Germany.
- McPherson, A., Tape, C., & Thurin, J., 2023. Regional Alaska earthquake moment tensors inverted using 3D Green’s functions, Abstract at 2023 SSA Annual Meeting, San Juan, Puerto Rico, 17–20 April.
- Montagner, J.-P. & Kennett, B. L. N., 1996. How to reconcile body-wave and normal-mode reference earth models, *Geophys. J. Int.*, **125**, 229–248.
- Myers, S. C., Ford, S. R., Mellors, R. J., Baker, S., & Ichinose, G., 2018. Absolute Locations of the North Korean Nuclear Tests Based on Differential Seismic Arrival Times and InSAR, *Seismol. Res. Lett.*, **89**(6), 2049–2058, doi: 10.1785/0220180123.
- Nissen-Meyer, T., Fournier, A., & Dahlen, F. A., 2007. A two-dimensional spectral-element method for computing spherical-earth seismograms – I. Moment-tensor source, *Geophys. J. Int.*, **168**, 1067–1092, doi: 10.1111/j.1365-246X.2006.03121.x.
- Nissen-Meyer, T., van Driel, M., Stähler, S. C., Hosseini, K., Hempel, S., Auer, L., Colombi, A., & Fournier, A., 2014. AxiSEM: broadband 3-D seismic wavefields in axisymmetric media, *Solid Earth*, **5**, 425–445, doi: 10.5194/se-5-425-2014.
- Pasyanos, M. E. & Myers, S. C., 2018. The Coupled Location/Depth/Yield Problem for North Korea’s Declared Nuclear Tests, *Seismol. Res. Lett.*, **89**(6), 2059–2067, doi: 10.1785/0220180109.
- Pham, T. S., Tkalcic, H., Hu, J., & Kim, S., 2024. Towards a new standard for seismic moment tensor inversion containing 3-D earth structure uncertainty, *Geophys. J. Int.*, **238**(3), 1840–1853, doi: 10.1093/gji/ggae256.
- Pham, T.-S. & Tkalcic, H., 2021. Toward improving point-source moment-tensor inference by incorporating 1D Earth model’s uncertainty: Implications for the Long Valley Caldera earthquakes, *J. Geophys. Res. Solid Earth*, **126**, 1–27, doi: 10.1029/2021JB022477.

- Pugh, D. J. & White, R. S., 2018. MTfit: A Bayesian Approach to Seismic Moment Tensor Inversion, *Seismol. Res. Lett.*, **89**(4), 1507–1513, doi: 10.1785/0220170273.
- Ramos-Martínez, J. & McMechan, G. A., 2001. Source-Parameter Estimation by Full Waveform Inversion in 3D Heterogeneous, Viscoelastic, Anisotropic Media, *Bull. Seismol. Soc. Am.*, **91**(2), 276–291, doi: 10.1785/0120000017.
- Riedesel, M. A. & Jordan, T. H., 1989. Display and assessment of seismic moment tensors, *Bull. Seismol. Soc. Am.*, **79**(1), 85–100.
- Rodriguez Cardozo, F. R., Braunmiller, J., Thompson, G., Graybeal, D., Thurin, J., Ding, L., Liu, Q., Modrak, R., & Tape, C., 2022. Seismic moment tensor estimation and uncertainty quantification in 1D and 3D Earth models using regional waveforms with application to the Middle East, in *AGU Fall Meeting Abstracts*, vol. 2022, pp. S13A–05.
- Sawade, L., Beller, S., Lei, W., & Tromp, J., 2022. Global centroid moment tensor solutions in a heterogeneous earth: the CMT3D catalogue, *Geophys. J. Int.*, **231**(3), 1727–1738, doi: 10.1093/gji/ggac280.
- Shearer, P. M., 2009. *Introduction to Seismology*, Cambridge U. Press, Cambridge, UK, 2nd edition.
- Silwal, V. & Tape, C., 2016. Seismic moment tensors and estimated uncertainties in southern Alaska, *J. Geophys. Res. Solid Earth*, **121**, 2772–2797, doi: 10.1002/2015JB012588.
- Stähler, S. C. & Sigloch, K., 2014. Fully probabilistic seismic source inversion – Part 1: Efficient parameterisation, *Solid Earth*, **5**, 1055–1069, doi: 10.5194/se-5-1055-2014.
- Stroujkova, A., 2018. Extracting the Source Spectra for the North Korean Nuclear Tests, *Seismol. Res. Lett.*, **89**(6), 2174–2182, doi: 10.1785/0220180125.
- Takemura, S., Okuwaki, R., Kubota, T., Shiomi, K., Kimura, T., & Noda, A., 2020. Centroid moment tensor inversions of offshore earthquakes using a three-dimensional velocity structure model: slip distributions on the plate boundary along the Nankai Trough, *Geophys. J. Int.*, **222**(2), 1109–1125, doi: 10.1093/gji/ggaa238.
- Tape, W. & Tape, C., 2012. A geometric setting for moment tensors, *Geophys. J. Int.*, **190**, 476–498, doi: 10.1111/j.1365-246X.2012.05491.x.

- Tape, W. & Tape, C., 2015. A uniform parameterization of moment tensors, *Geophys. J. Int.*, **202**, 2074–2081, doi: 10.1093/gji/ggv262.
- Tape, W. & Tape, C., 2016. A confidence parameter for seismic moment tensors, *Geophys. J. Int.*, **205**, 938–953, doi: 10.1093/gji/ggw057.
- Tape, W. & Tape, C., 2019. The eigenvalue lune as a window on moment tensors, *Geophys. J. Int.*, **216**, 19–33, doi: 10.1093/gji/ggy373.
- Thurin, J. & Tape, C., 2023. Comparison of force and moment tensor estimations of subevents during the 2022 Hunga–Tonga submarine volcanic eruption, *Geophys. J. Int.*, **235**, 1959–1981, doi: 10.1093/gji/ggad323.
- Thurin, J., Tape, C., & Modrak, R., 2022. Multi-event explosive seismic source for the 2022  $M_w$  6.3 Hunga Tonga submarine volcanic eruption, *The Seismic Record*, **2**(4), 217–226, doi: 10.1785/0320220027.
- Tian, D., Yao, J., & Wen, L., 2018. Collapse and Earthquake Swarm After North Korea’s 3 September 2017 Nuclear Test, *Geophys. Res. Lett.*, **45**(9), 3976–3983, doi: <https://doi.org/10.1029/2018GL077649>.
- Tian, D., Uieda, L., Leong, W. J., Schlitzer, W., Fröhlich, Y., Grund, M., Jones, M., Toney, L., Yao, J., Magen, Y., Tong, J.-H., Materna, K., Belem, A., Newton, T., Anant, A., Ziebarth, M., Quinn, J., & Wessel, P., 2024. PyGMT: A Python interface for the Generic Mapping Tools, doi: 10.5281/zenodo.10578540.
- Vackář, J., Burjánek, J., Gallovič, F., Zahradník, J., & Clinton, J., 2017. Bayesian ISOLA: new tool for automated centroid moment tensor inversion, *Geophys. J. Int.*, **210**(2), 693–705, doi: 10.1093/gji/ggx158.
- Valentine, A. P. & Trampert, J., 2012. Assessing the uncertainties on seismic source parameters: Towards realistic error estimates for centroid-moment-tensor determinations, *Phys. Earth Planet. Inter.*, **210–211**, 36–49, doi: 10.1016/j.pepi.2012.08.003.
- van Driel, M., Krischer, L., Stähler, S. C., Hosseini, K., & Nissen-Meyer, T., 2015. Instaseis: instant global seismograms based on a broadband waveform database, *Solid Earth*, **6**, 701–717, doi: 10.5194/se-6-701-2015.

- Walter, W. R., Dodge, D. A., Ichinose, G., Myers, S. C., Pasyanos, M. E., & Ford, S. R., 2018. Body-Wave Methods of Distinguishing between Explosions, Collapses, and Earthquakes: Application to Recent Events in North Korea, *Seismol. Res. Lett.*, **89**(6), 2131–2138, doi: 10.1785/0220180128.
- Wang, T., Shi, Q., Nikkhoo, M., Wei, S., Barbot, S., Dreger, D., Bürgmann, R., Motagh, M., & Chen, Q.-F., 2018. The rise, collapse, and compaction of Mt. Mantap from the 3 September 2017 North Korean nuclear test, *Science*, **361**, 166–170, doi: 10.1126/science.aar7230.
- Wessel, P. & Smith, W. H. F., 1991. Free software helps map and display data, *Eos Trans. Am. Geophys. Un.*, **72**(41), 441 ff.
- West, M. E., Bender, A., Gardine, M., Gardine, L., Gately, K., Haeussler, P., Hassan, W., Meyer, F., Richards, C., Ruppert, N. A., Tape, C., Thornley, J., & Witter, R., 2019. The 30 November 2018  $M_w$  7.1 Anchorage earthquake, *Seismol. Res. Lett.*, **91**(1), 66–84, doi: 10.1785/0220190176.
- Xu, J., Zhang, W., Liang, X., Rong, J., & Li, J., 2021. Joint microseismic moment-tensor inversion and location using P- and S-wave diffraction stacking, *GEOPHYSICS*, **86**(6), KS137–KS150, doi: 10.1190/geo2021-0104.1.
- Yagi, Y. & Fukahata, Y., 2011. Introduction of uncertainty of Green's function into waveform inversion for seismic source processes, *Geophys. J. Int.*, **186**(2), 711–720, doi: 10.1111/j.1365-246X.2011.05043.x.
- Yao, J., Tian, D., Sun, L., & Wen, L., 2018. Source Characteristics of North Korea's 3 September 2017 Nuclear Test, *Seismol. Res. Lett.*, **89**(6), 2078–2084, doi: 10.1785/0220180134.
- Zhao, L.-S. & Helmberger, D. V., 1994. Source estimation from broadband regional seismograms, *Bull. Seismol. Soc. Am.*, **84**(1), 91–104.
- Zhu, L. & Ben-Zion, Y., 2013. Parameterization of general seismic potency and moment tensors for source inversion of seismic waveform data, *Geophys. J. Int.*, **194**, 839–843, doi: 10.1093/gji/ggt137.

Zhu, L. & Helmberger, D., 1996. Advancement in source estimation techniques using broadband regional seismograms, *Bull. Seismol. Soc. Am.*, **86**(5), 1634–1641.

Zhu, L. & Rivera, L. A., 2002. A note on the dynamic and static displacements from a point source in multilayered media, *Geophys. J. Int.*, **148**, 619–627, doi: 10.1046/j.1365-246X.2002.01610.x.

**Table 1.** Numerical solvers supported by MTUQ for the computation of Green's functions databases.

| Supported solver                               | Numerical method            | Type of model  | High-performance computing features                               | Notes  |
|--|-----------------------------|--|---|--|
| AxiSEM   | Spectral element method     | Axisymmetric/ radially symmetric                           | OpenMP parallelization, parallel I/O                              | Preferred solver for 1D models   |
| FK   | Frequency-wavenumber method | Horizontally layered                                       | N/A   | Suited for local scales  |
| SPECFEM3D/<br>3D_GLOBE<br>(source-side mode)   | Spectral element method     | Fully 3D   | Hybrid MPI+OpenMP parallelization, GPU acceleration, parallel I/O | Green's functions stored at individual stations  |
| SPECFEM3D/<br>3D_GLOBE<br>(receiver-side mode) | Spectral element method     | Fully 3D   | Hybrid MPI+OpenMP parallelization, GPU acceleration, parallel I/O | Green's functions stored over source volume; implementation based on reciprocity theorem |
| Syngine precomputed databases                  | N/A                         | Limited selection of radially symmetric whole-Earth models | N/A   | Precomputed synthetics available for download via web service                            |

**Table 2.** Datasets used to determine the DPRK6 source type for a subset of published studies.

| Study                   | P/S ratio | Regional body | Regional surface | Regional polarities | Teleseismic polarities | Static deformation |
|-------------------------|-----------|---------------|------------------|---------------------|------------------------|--------------------|
| Yao et al. (2018)       |           |               | ✓                |                     |                        |                    |
| Walter et al. (2018)    | ✓         |               |                  |                     |                        |                    |
| Wang et al. (2018)      |           | ✓             | ✓                |                     |                        |                    |
| Liu et al. (2018)       |           |               | ✓                |                     |                        |                    |
| Chiang et al. (2018)    |           |               | ✓                | ✓                   | ✓                      |                    |
| Alvizuri & Tape (2018)  |           |               | ✓                | ✓                   |                        |                    |
| Hong et al. (2019)      |           |               | ✓                |                     |                        |                    |
| Chi-Durán et al. (2021) |           |               | ✓                | ✓                   | ✓                      | ✓                  |
| Hu et al. (2023)        |           |               | ✓                |                     |                        |                    |
| Chi-Durán et al. (2024) |           |               | ✓                | ✓                   | ✓                      | ✓                  |
| Hu et al. (2024)        |           |               |                  |                     |                        |                    |
| This study              | ✓         | ✓             | ✓                | ✓                   | ✓                      |                    |

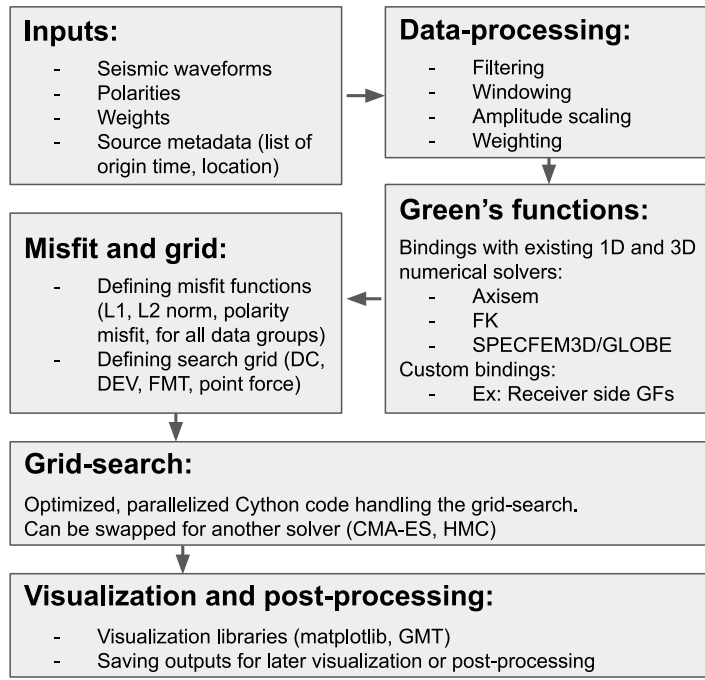


**Figure 1.** Schematic representation of MTUQ’s code structure. The modular nature of the code is depicted by interconnected boxes, each representing a default tool that can be swapped out for alternative external libraries as needed. Modules in this flowchart can be replaced or extended via function and method overloading. CMA-ES refers to the Covariance Matrix Adaptation Evolution Strategy by Hansen & Ostermeier (2001), and HMC refers to Hamiltonian Monte-Carlo (Duane et al., 1987), two external solvers tested in conjunction with MTUQ.

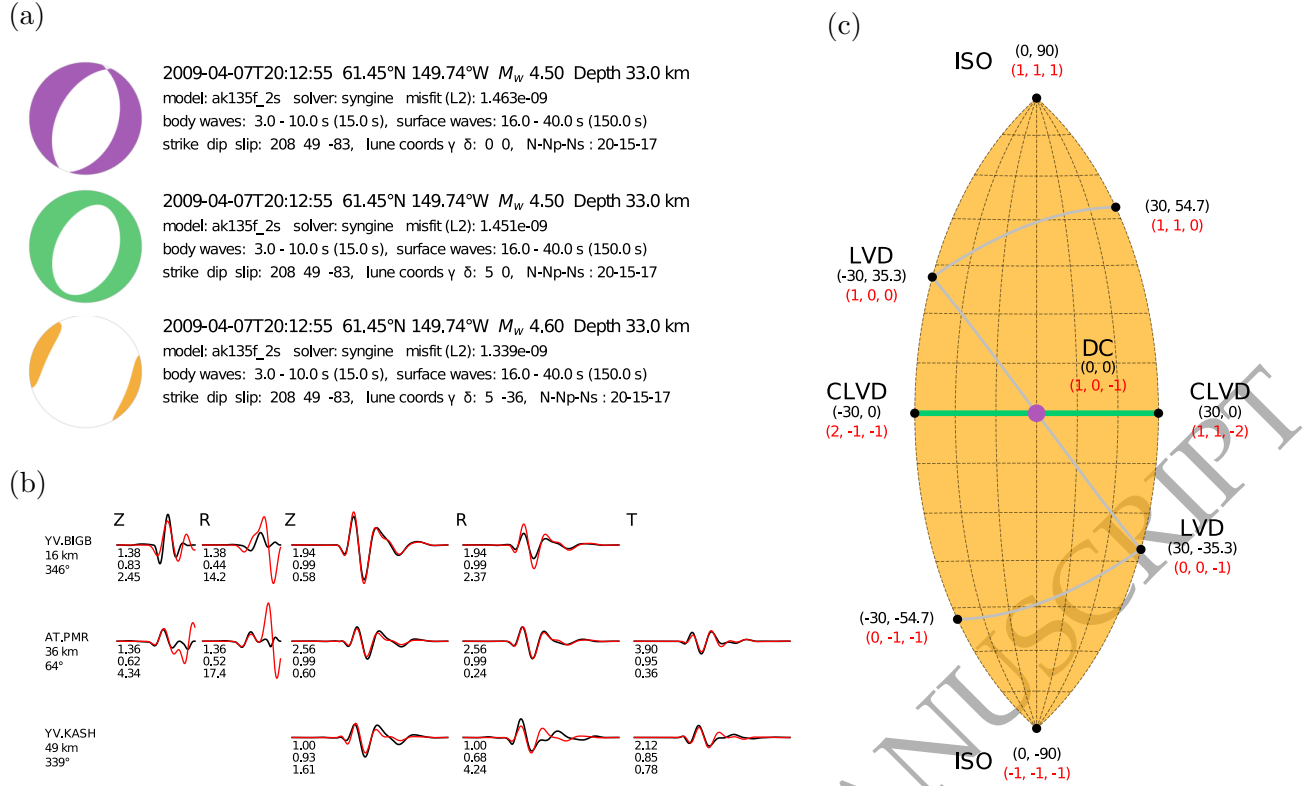


**Figure 2.** Fundamental visualization utilities for MTUQ. (a) Waveform misfit plot headers for three inversions: double couple (DC, purple), deviatoric (DEV, green), and full moment tensor (FULL, yellow). Each header includes the event's origin time, location, magnitude, depth, model, solver, and misfit (L2). Location, depth, and magnitude can be estimated during inversion. Additional details include body and surface wave time windows, strike, dip, and slip angles, and lune coordinates ( $\gamma$ ,  $\delta$ ), along with the number of stations used: total number (N), stations used for the P-waves component (Np), and stations used for the surface waves component (Ns). (b) A subset of observed and synthetic waveforms for three out of 20 stations, displayed for the full moment tensor inversion. The five columns represent P-waves (Z, R), Rayleigh waves (Z, R), and Love waves (T), with vertical (Z), radial (R), and transverse (T) components. Each waveform is labeled with three values: best time-shift in seconds, normalized cross-correlation coefficient, and contribution to the misfit (percentage). (c) Moment tensor source type depicted using the eigenvalue lune. Three grid subsets are color-coded to correspond with DC (purple), DEV (green), and FULL (yellow) shown in (a). Reference source types on the lune are indicated by black dots, with their corresponding longitude and latitude (black) and unnormalized eigenvalue triple (red). ISO denotes isotropic sources, LVD represents linear-vector-dipoles, CLVD stands for compensated linear-vector-dipoles, and DC represents double-couple solutions.

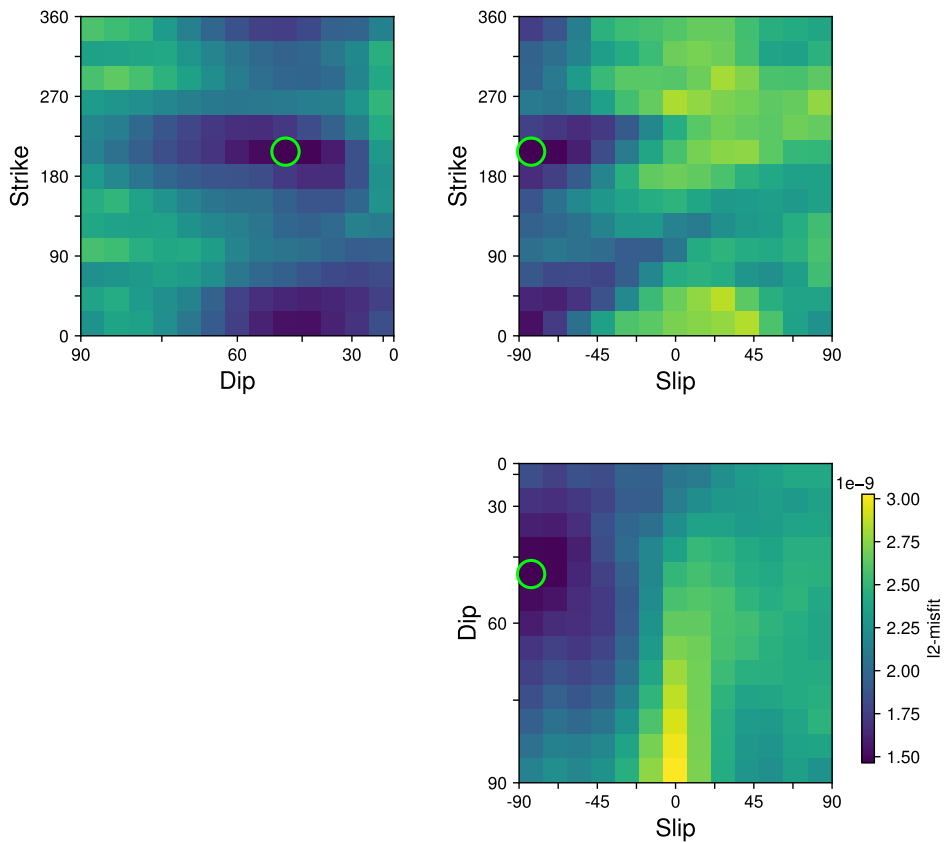


**Figure 3.** Waveform misfit plotted as a function of orientation parameters: (top left) strike vs. dip, (top right) strike vs. slip, and (bottom) dip vs. slip. In this example, the moment tensor is constrained to be a double couple. The green circles indicate the best-fitting solution (optimal orientation/angular triplet) in the parameter space, which is strike  $\kappa = 208^\circ$ , dip  $\theta = 49^\circ$ , and slip (rake)  $\sigma = -83^\circ$ . Each map quadrant only shows the best misfit value for each parameter pair by aggregating the best-fitting solutions across the third parameter and magnitude.

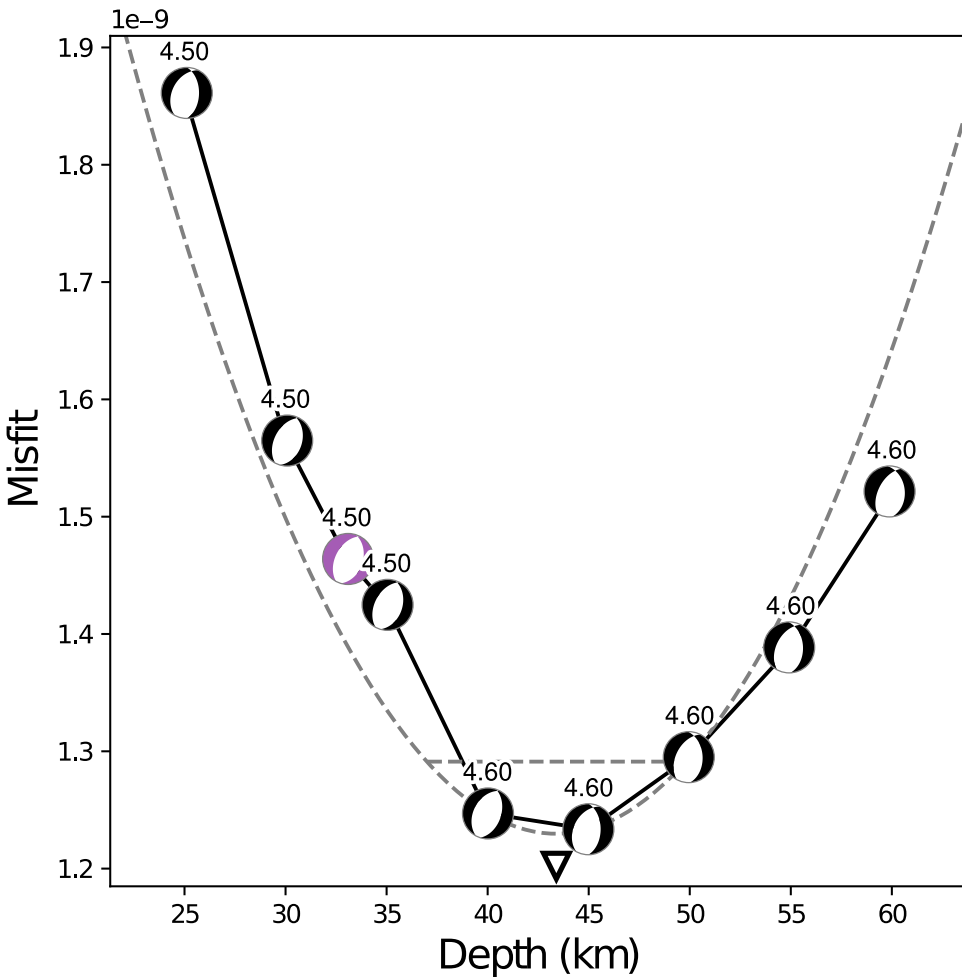


**Figure 4.** Waveform misfit as a function of depth for the double-couple-constrained moment tensor inversion. The best-fitting moment tensor and magnitude at each depth are displayed along the curve. The variation in misfit with depth provides insight into the optimal source depth for this event based on waveform fitting and a given earth model. Each source depth is associated with a complete misfit volume with respect to orientation as in Figure 3, as the whole grid search is applied to each source depth. The dashed parabola is derived from interpolation of the three best-fitting points, to obtain an estimate of the best depth (inverted triangle at 43.4 km), as well as to provide an uncertainty estimate ( $\pm 6.4$  km for the values within 5% of the minimum). The depth search increment is  $\Delta z = 5$  km, and the magnitude search increment is  $\Delta M_w = 0.1$ . The depth of 33 km was added to the grid, in order to showcase the overlap between grids. The best-fitting moment tensor at 33 km depth is identical to the solution of Figure 2 and is color-coded accordingly.

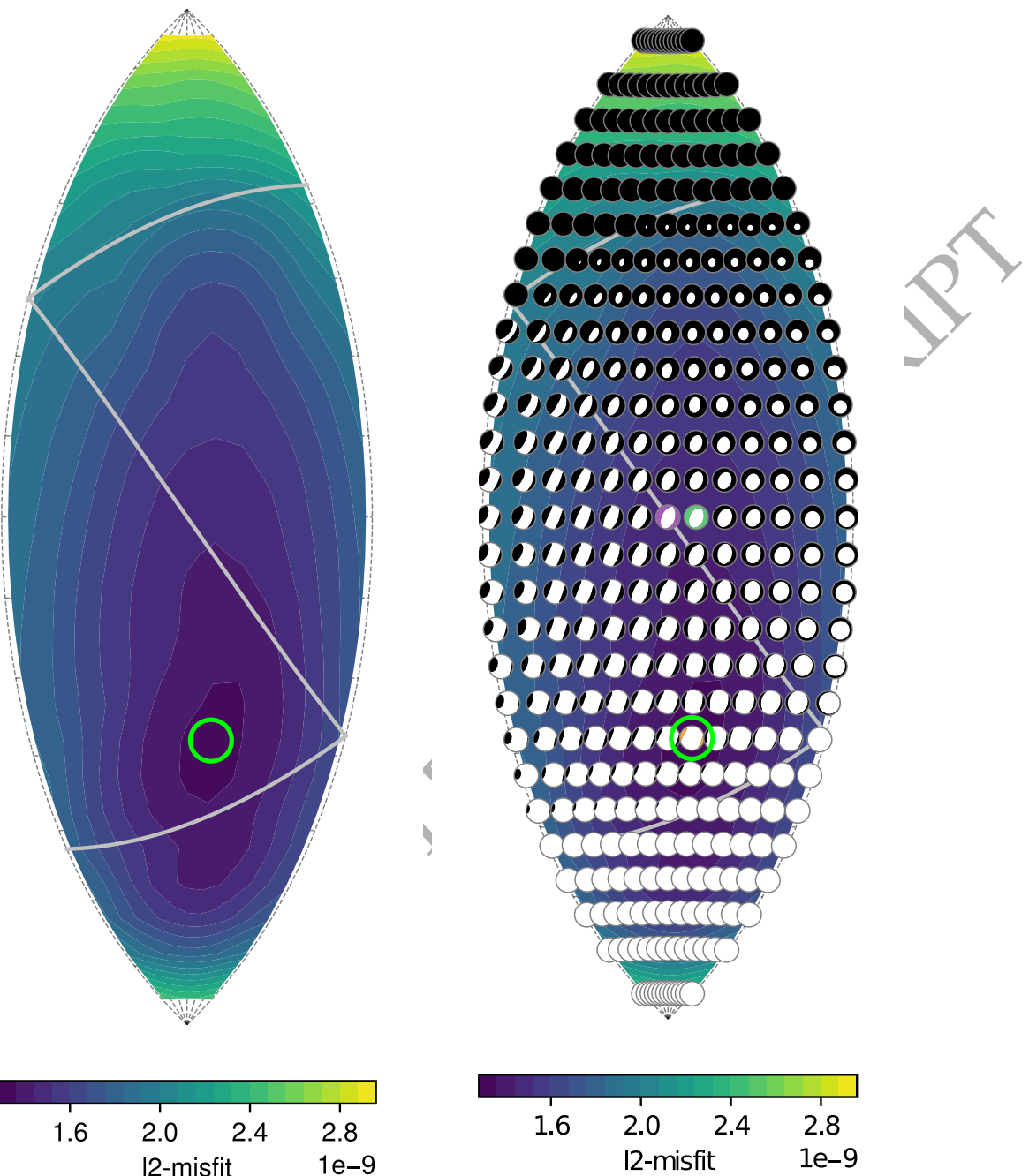


**Figure 5.** Misfit map plotted on the eigenvalue lune (Figure 2c). The green circle depicts the best-fitting source type coordinates: lune longitude  $\gamma = 5^\circ$ , lune latitude  $\delta = -36^\circ$ . The map shows only the best misfit value for each location on the lune, aggregated from the lowest misfit values across all orientations and magnitudes for a fixed source type, similar to the approach used for double-couple misfit maps. The depth is fixed at 33 km. The misfit map on the lune shows the best-fitting moment tensor for each source type. The double-couple and deviatoric tensor solutions from Figure 2 are included in the full moment tensor grid and are highlighted using the same color code as in Figure 2.

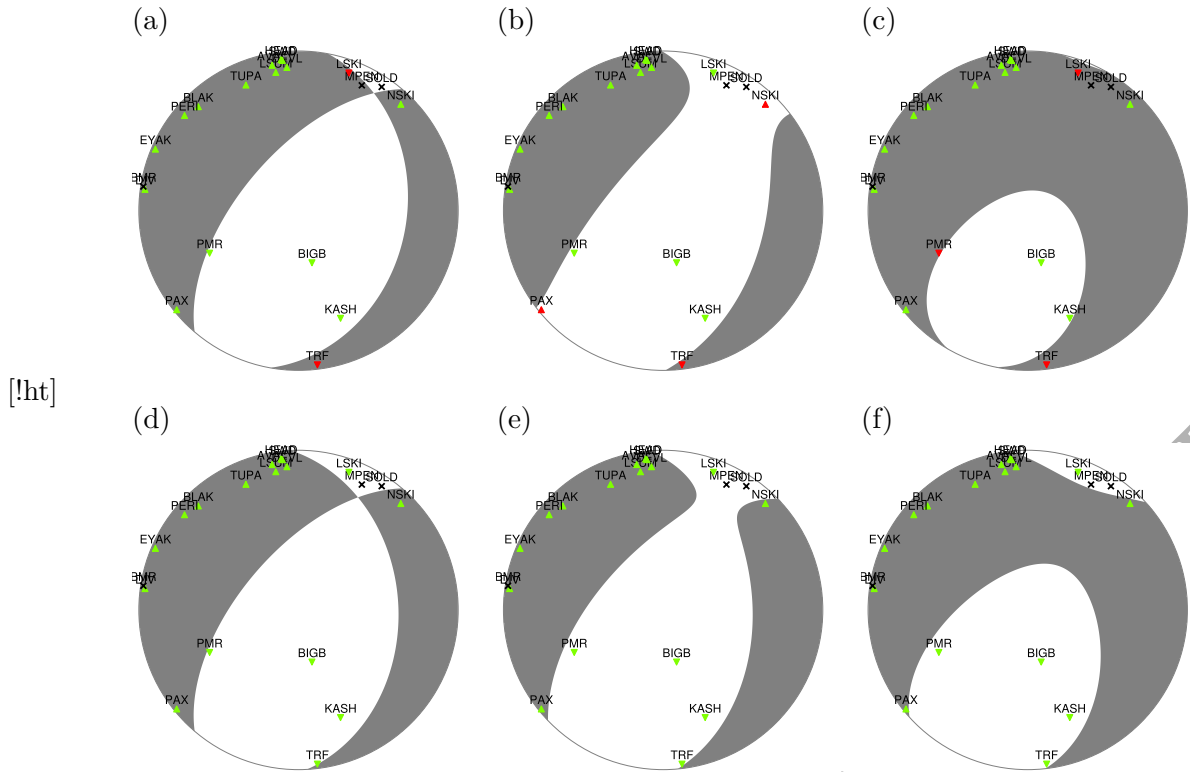
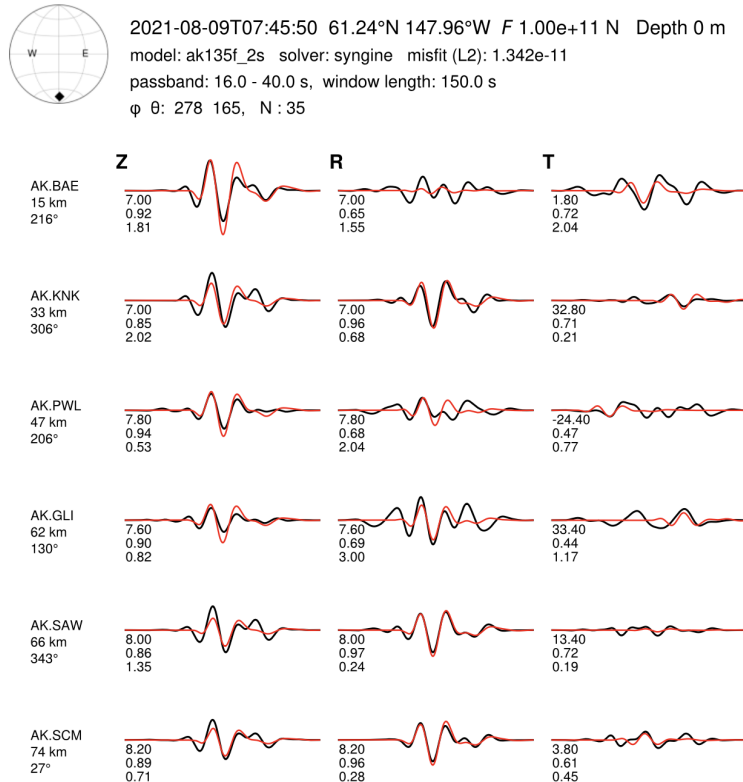


**Figure 6.** The influence of first-motion polarity measurements. (a)-(c) Results for P-waves and surface waves only ( $\alpha = 1$  in equation 8) for (a) double-couple, (b) deviatoric, and (c) full moment tensor inversions. Green triangles indicate stations where predicted and observed first-motion polarities match, red triangles indicate mismatches, and black crosses mark stations where data were available but no first-motion data were used. Triangle positions on the focal-sphere are determined by azimuth to the station and takeoff angle, computed using the ak135f model. (d)-(f) Results incorporating both waveform and polarity data ( $\alpha = 0.5$  in equation 8) for (d) double-couple, (e) deviatoric, and (f) full moment tensor inversions.

(a)



(b)

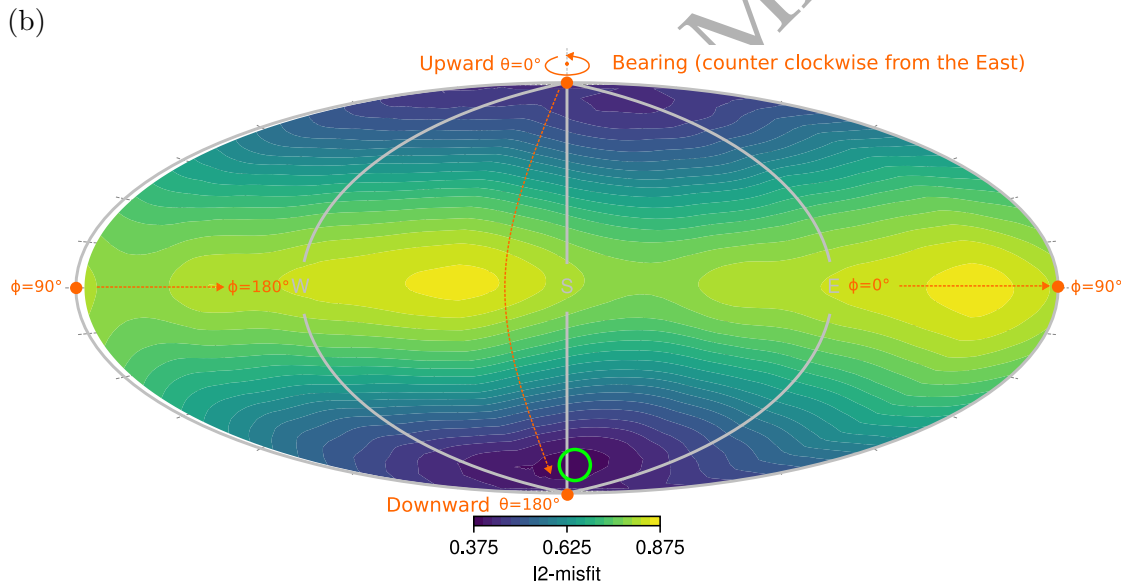


**Figure 7.** Waveform misfit plots for a point-force inversion of the 2021 Barry Arm landslide event. (a) Waveform misfit plot comparing observed (black) and synthetic (red) waveforms generated by a best-fitting point force. The best-fitting force direction ( $\phi = 278^\circ$ ,  $\theta = 165^\circ$ ) points predominantly downward; it is marked by a black diamond on the unwrapped sphere. A subset of 7 stations from the 35 used in the inversion is shown. (b) Waveform misfit map plotted on the unit sphere. Cardinal directions are labeled as W (west) and E (east) along their respective meridians. The southern direction is located along the central meridian labeled as S, and the northern direction is on the boundary of the ellipse. A green circle marks the best-fitting force direction.

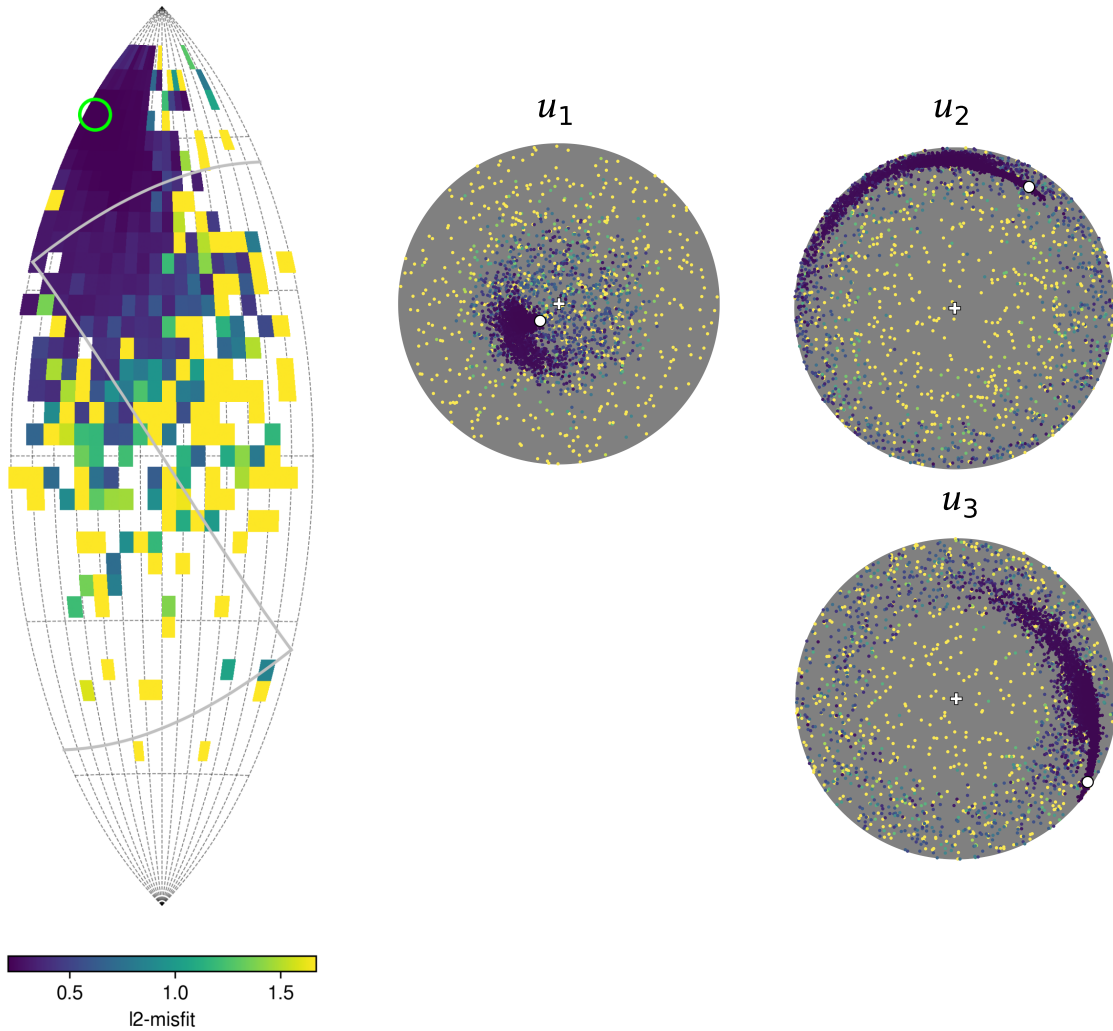


**Figure 8.** Misfit maps for the moment tensor inversion using CMA-ES for the 2017 DPRK nuclear event. On the left, misfit values are plotted over the eigenvalue lune (Figure 2c). The misfit values are binned into regularly spaced cells, and only the minimum misfit value in each cell is shown, considering all possible magnitudes. The right panels display the orientation of the best-fitting moment tensor, represented by the three principal axes:  $\mathbf{U} = [\mathbf{u}_1, \mathbf{u}_2, \mathbf{u}_3]$ . The scatter of all sampled principal axes from the 11,520 CMA-ES samples is colored by misfit, with the principal axes of the best-fitting tensor highlighted by solid white circles. The center of each beachball is marked by a white cross for reference. The vector  $\mathbf{u}_1$  is the T-axis,  $\mathbf{u}_2$  is the B-axis, and  $\mathbf{u}_3$  is the P-axis. For this inversion, the best-fitting magnitude is  $M_w$  5.44, the depth is fixed to 1 km, and the assumed Earth model is the MDJ2 model.

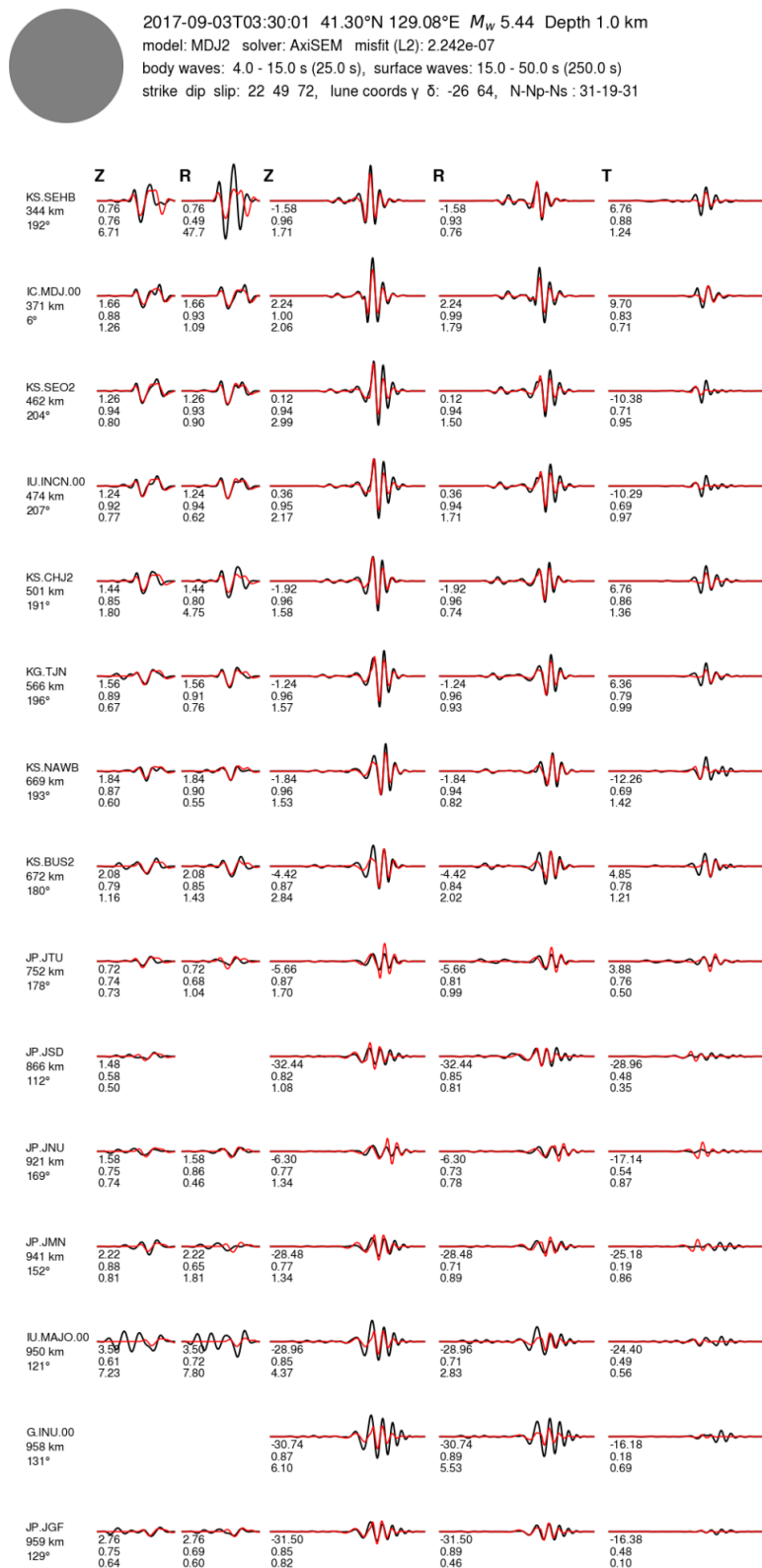


**Figure 9.** Waveform misfit plot for the 2017 DPRK nuclear event. The best-fitting moment tensor has a source type with lune longitude  $\gamma = -26^\circ$  and lune latitude  $\delta = 64^\circ$ , as shown in Figure 10 [BW,SW,RP,TP]. A subset of waveforms from 15 out of 31 stations is displayed. See Section 4.3.3 for details.

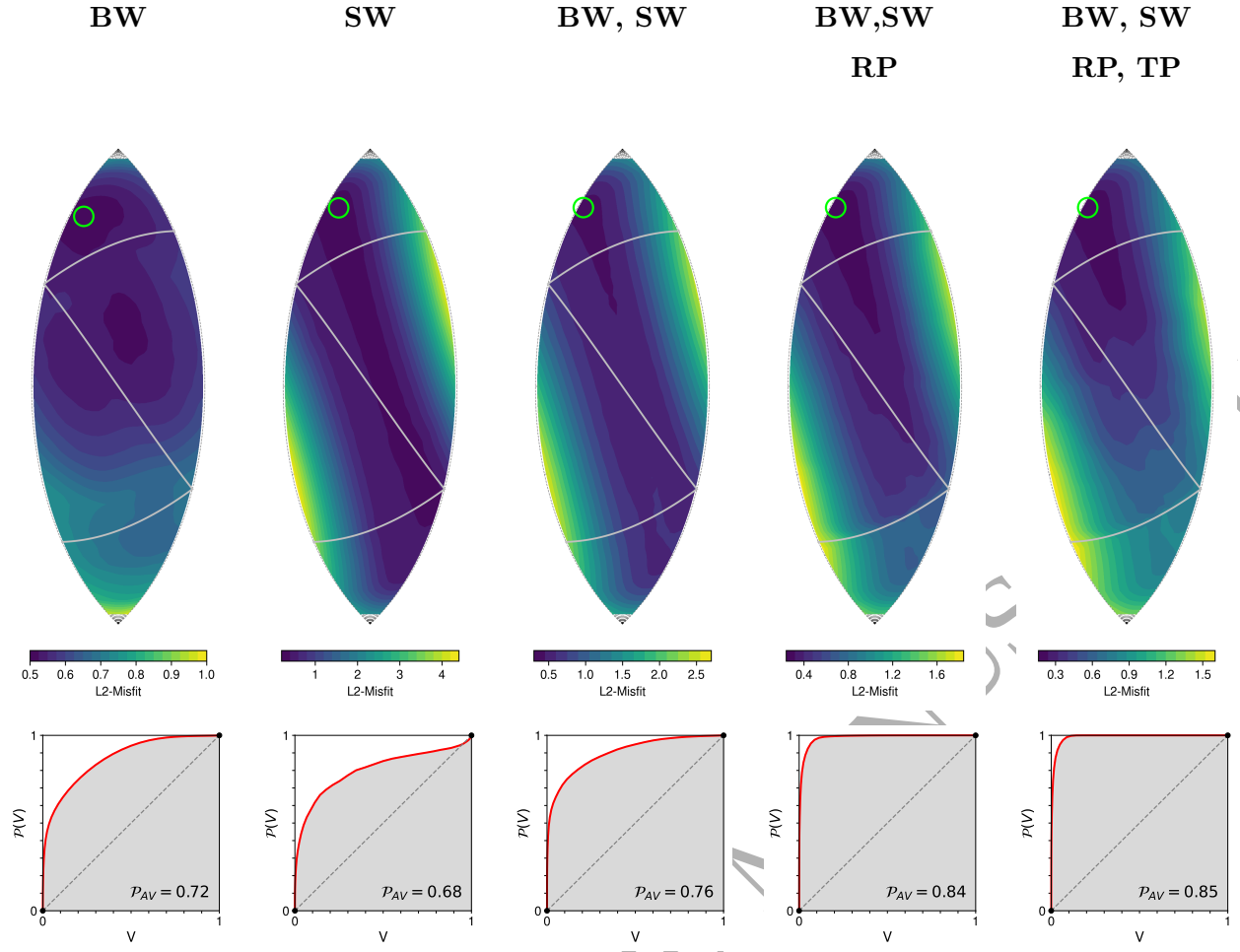
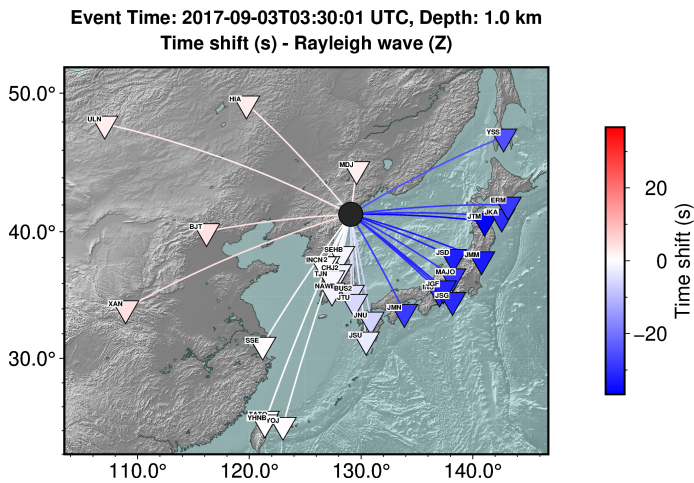


**Figure 10.** The influence of different data types on the moment tensor estimated for the 2017 DPRK nuclear event. Each eigenvalue lune (Figure 2c) shows the waveform misfit for a different combination of data. The best-fitting solution for each map is depicted by a green circle. The four data sets considered are BW = body waves, SW = surface waves, RP = regional first-motion polarities, and TP = teleseismic first-motion polarities. The five misfit maps display combinations of these data sets, ranging from body waves only (left) to all four combined (right). In each map, the misfit is normalized by the corresponding data norm used in the inversion. Equal weights are assigned to each data group to ensure balanced contributions in the joint inversions. For example, when all four data groups are used, the corresponding misfit weights are [0.25, 0.25, 0.25, 0.25]. Below each misfit map is plotted the corresponding confidence curve over the solution space volume  $V$ , as described in Tape & Tape (2016). Waveform fits for each case can be found in Figures S14 to S25, with a subset for the joint inversion [BW,SW,RP,TP] displayed in Figure 9.

(a) Rayleigh (Z,R)



(b) Love (T)

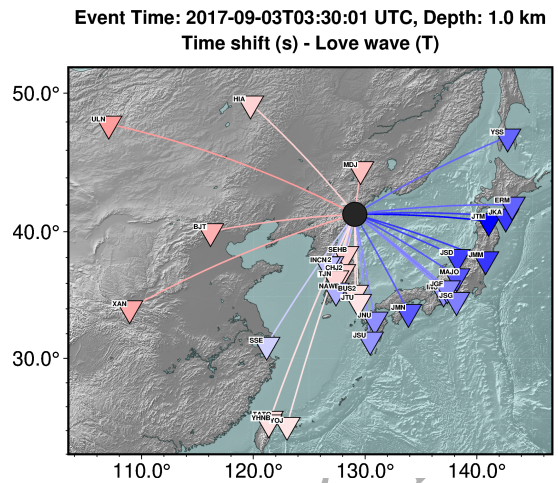


**Figure 11.** Surface wave time-shift maps for the 2017 DPRK best-fitting moment tensor. A subset of the corresponding waveforms is shown in Figure 9. The azimuthal pattern in time shifts reflects differences between the Earth structure in the assumed 1D model (MDJ2) and the actual Earth structure. The significant negative time shifts toward Japan indicate that the MDJ2 model—designed for the continental path to station MDJ—is too slow to accurately model fast propagation through oceanic paths. (a) Rayleigh wave time shifts measured on the vertical and radial components. (b) Love wave time shifts measured on the transverse component.